國立臺灣大學電機資訊學院光電工程學研究所

碩士論文

Graduate Institute of Photonics and Optoelectronics

College of Electrical Engineering and Computer Science

National Taiwan University

Master Thesis

在量子井結構上表面奈米孔洞內膠體量子點的發光、福斯特共振能量轉換與表面電漿子耦合行為

Emission, Förster Resonance Energy Transfer and Surface Plasmon Coupling Behaviors of Colloidal Quantum Dots in a Surface Nanoscale Hole on a Quantum-well Structure

賴易承

Yi-Chen Lai

指導教授：楊志忠 博士

Advisor: Chih-Chung Yang, Ph.D.

中華民國 111 年 09 月

September 2022

doi:10.6342/NTU202203112

國立臺灣大學碩士學位論文
口試委員會審定書

在量子井結構上表面奈米孔洞內
膠體量子點的發光、福斯特共振能量轉換
與表面電漿子耦合行為
Emission, Förster Resonance Energy Transfer and Surface Plasmon Coupling Behaviors of Colloidal Quantum Dots in a Surface Nanoscale Hole on a Quantum-well Structure

本論文係賴易承君（學號 R08941097）在國立臺灣大學光電工程學研究所完成之碩士學位論文，於民國 111 年 9 月 1 日承下列考試委員審查通過及口試及格，特此證明

口試委員：楊志忠（指導教授）

林建中　　郭仰

黃建璋　　連英吉

所　長　吳肇欣

doi:10.6342/NTU202203112

誌謝

首先我要感謝我的父母，從小撫養教育及拉拔我長大，教會了我做人處事的道理，在背後的支持及鼓勵，並讓我在求學的這一路上，毫無後顧之憂，可以專注在課業及研究上。

接著，要感謝我的指導教授楊志忠博士，在碩班這段時間的教導，不只讓我在專業領域上更進一步，也讓我在人生這條路上學到了很多，一輩子受用無窮，在此獻上最深的感謝。

最後我要感謝在碩士班的所有同仁，特別是揚少波學長在量子井機板的提供，及吳順翔同學和林育聖學弟在光學量測上的幫忙，和馮璽宇學弟在合成銀奈米顆粒及光阻的幫助，謝謝你們的幫助，得已讓我完成此篇論文，並能順利取得碩士學位。

doi:10.6342/NTU202203112

中文摘要

我們將膠體量子點和化學合成的銀奈米顆粒連同光阻填入貫穿整個量子井結構的表面奈米孔洞中，顯示量子點發光、從綠光量子點到紅光量子點之間的福斯特共振能量轉換、從量子井到量子點之間的福斯特共振能量轉換效率可以提升，而表面電漿子耦合的效果也明顯上升。在本研究中，我們首先探討在沒有量子井結構內的結果，為此我們將奈米洞的陣列製作在的氮化鎵模板上，接著，才將奈米洞的陣列製作在有銦氮化鎵/氮化鎵量子井的基板上，探討量子井與量子點之間福斯特共振能量轉換的行為。在這兩種不同的模板上，我們比較表面製作奈米洞陣列的樣品與表面為平面的樣品之結果，同時也比較兩種不同深度的奈米洞樣品，這幾種樣品，其奈米洞都貫穿量子井結構。較淺的奈米洞樣品顯示從量子井到量子點之間的整體福斯特共振能量轉換效率比較高。此外，我們也探討了比量子井更淺的奈米洞樣品，在其表面鋪上由銀奈米顆粒和量子井產生的表面電漿子耦合，來探討量子井到量子點之間的福斯特共振能量轉換之變化，結果顯示藉由表面電漿子耦合的效果可以增強福斯特共振能量轉換的效率。

doi:10.6342/NTU202203112

Abstract:

The enhancements of colloidal quantum dot (QD) emission, Förster resonance energy transfer (FRET) from green-emitting QD (GQD) into red-emitting QD (RQD), FRET from embedded quantum well (QW) into QD, and surface plasmon (SP) coupling effect when QDs and synthesized Ag nanoparticles (NPs) are inserted into a surface nano-hole, which penetrates through the whole QW structure, are demonstrated. Nano-hole arrays on a GaN template to understand the effects without QW are first fabricated. Then, nano-hole arrays on an InGaN/GaN QW template for studying the FRET processes from the QW into QD are prepared. The samples with planar top surfaces for overlaying colloidal QDs are also fabricated to compare the results with the nano-hole samples. Meanwhile, the results of a set of sample with deeper nano-holes are compared with those with shallower nano-holes. The overall FRET from the QW structure into the inserted QDs in a shallower nano-hole sample is stronger. Besides, the SP coupling effect of surface Ag NPs on the FRET from the QW structure into the QDs inserted into a shallow nano-hole is investigated. The FRET process can be enhanced through the SP coupling effect.

doi:10.6342/NTU202203112

Contents

doi:10.6342/NTU202203112

doi:10.6342/NTU202203112

doi:10.6342/NTU202203112

List of Figure

doi:10.6342/NTU202203112

doi:10.6342/NTU202203112

doi:10.6342/NTU202203112

doi:10.6342/NTU202203112

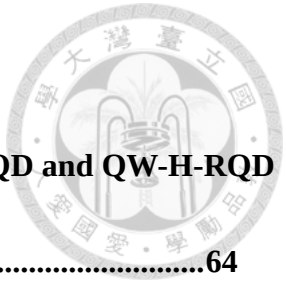

doi:10.6342/NTU202203112

doi:10.6342/NTU202203112

doi:10.6342/NTU202203112

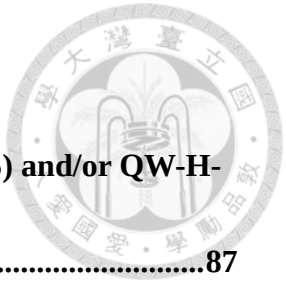

doi:10.6342/NTU202203112

doi:10.6342/NTU202203112

List of Table

doi:10.6342/NTU202203112

doi:10.6342/NTU202203112

Chapter 1 Introduction

1.1 Photon down-conversion and Förster resonance energy transfer

Photon down-conversion is an effective method for generating the light of a new color, particularly when the fabrication of a high-efficiency light emitter for this color is difficult [1, 2]. As an example, for yellow light generation, it is usually difficult to use either InGaN or AlGaInP material system for achieving a high emission efficiency [3, 4]. Yellow light generation based on a color conversion process through colloidal quantum dots (QDs) can be a useful approach to achieve a higher emission efficiency. Color conversion is also useful for implementing the arrayed pixels of different emitting colors in display application [5, 6]. Green- and red-emitting QDs can be placed in different pixels on a blue-emitting LED base to convert blue light into the designated colors. A color conversion process is realized through the acceptor absorption of the emitted photons from the donor and then the emission of the acceptor. However, the color conversion efficiency of such a far-field process is limited by the absorption cross section of the acceptor. If the distance between the donor and acceptor can be reduced to a scale of tens nm, the acceptor can absorb the energy of the strong near field produced by the donor, resulting in a higher absorption efficiency and hence a more effective color conversion process. With the development of the nano-process technology, such a near-field interaction, known as the Förster resonance energy transfer (FRET) [7-11], becomes feasible for color conversion application.

1.2 Colloidal quantum dots in surface nano-holes for enhancing Förster resonance energy transfer

To implement an nm-scale distance between a donor and an acceptor, the insertion of the donor

doi:10.6342/NTU202203112

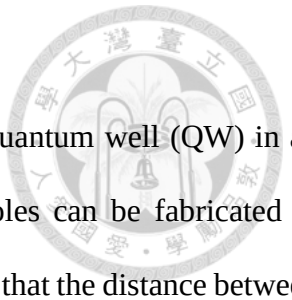

and/or acceptor into a nanoscale cavity is an attractive method. When a quantum well (QW) in an LED serves as the donor in an energy transfer process, surface nano-holes can be fabricated to penetrate through the QW structure for inserting color-converting QDs such that the distance between an inserted QD and the portion of the QW near the nano-hole sidewall is small for producing FRET and hence enhancing color conversion [12-17]. In such an implementation, the FRET effect has been claimed typically based on the observations of a higher color conversion efficiency and a shorter (longer) photoluminescence (PL) decay time of the donor (acceptor) emission, when compared with a reference sample of overlaying QDs onto a planar-surface LED. These observations are interpreted simply as the results of the short distance between the QDs in the nano-holes and the QW. However, such an interpretation oversimplifies the near-field interactions in such a nanoscale-cavity structure. Other important mechanisms exist in such a surface nano-hole with inserted QDs and nearby QWs for enhancing color conversion. The understanding of such mechanisms will help us in developing novel techniques for further improving the color conversion efficiency.

1.3 Surface plasmon coupling enhanced color conversion

When a light emitter or absorber is placed within the SP-resonance induced near-field distribution range of a metal nanostructure, SP coupling can enhance its emission or absorption efficiency [18-22]. In an SP coupling process for emission enhancement, the radiative recombination rate of a light emitter can be enhanced when a strong electromagnetic field at the emission wavelength is applied to the location of the light emitter [23]. In this process, carrier energy in the light emitter can be transferred into SP resonance for radiation such that the non-radiative recombination rate in the light emitter can be reduced, leading to a higher emission efficiency [24]. SP coupling has been used for improving the performance of an LED, including the enhancements of internal quantum efficiency

doi:10.6342/NTU202203112

(IQE) and electroluminescence intensity, the suppression of the efficiency droop effect, and the increase of LED modulation bandwidth [25-27]. SP coupling has also been used to enhance sunlight harvest in a photovoltaic device [21, 22]. Therefore, SP coupling can be used for enhancing the efficiencies of the three mechanisms mentioned in the last paragraph for a color conversion process. In particular, when the donor, acceptor, and the metal nanostructure for inducing SP resonance are close-by, the SP resonance excited by the donor can directly transfer energy into the acceptor through a three-body coupling process. This energy transfer process can effectively enhance the color conversion efficiency. SP-coupling enhanced color conversion from a blue-emitting QW structure or LED into red emission through colloidal QDs has been studied in experiment and numerical simulation based on the localized surface plasmon (LSP) resonances of Ag NPs [28-30, 31].

1.4 Preliminary study [32]

Red-emitting QDs immersed in a photoresist are inserted into the surface nano-holes fabricated on the p-type mesa of a blue-emitting QW LED to show an enhanced color conversion efficiency and an increased modulation bandwidth. Based on the TRPL study of the inserted QDs in a nano-hole structure fabricated on an un-doped GaN template of no QW, it is found that the radiative recombination rate of the inserted QDs is significantly increased due to the nanoscale-cavity effect. This effect can also enhance the FRET efficiency when QDs are inserted into a nano-hole structure fabricated in an LED. Simulation studies confirm the enhancements of dipole radiation efficiency and FRET when it is placed in a nano-hole structure. Although FRET has been regarded as the major cause for increasing the color conversion efficiency of the QDs inserted into such a surface nano-hole structure in an LED, the study results show that the nanoscale-cavity effect plays a more important role. Figure 1.1 schematically shows the structures of the samples under study. Here, with surface

doi:10.6342/NTU202203112

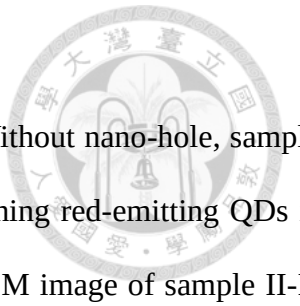

nano-holes, samples II-H and II-H-Q are fabricated based on sample II. Without nano-hole, sample I-Q is fabricated based on sample I. A photoresist (SU-8) solution containing red-emitting QDs is applied to sample I-Q and II-H-Q. Figure 1.2(a) shows the plane-view SEM image of sample II-H with the region circled by the red rectangle being magnified to show the SEM image in Fig. 1.2(b). Figures 1.2(c) and 1.2(d) show the cross-sectional SEM images of a nano-hole array before and after the application of the photoresist solution, respectively. Figure 1.3 shows the ratios of red intensity over blue intensity (R/B ratio) of samples I-Q and II-H-Q (with the left ordinate) and the R/B ratio enhancement (with the right ordinate) of sample II-H-Q with respect to that of sample I-Q. Figure 1.4 shows the TRPL decay profiles of the QW and QD emissions in the samples with nano-holes and inserted QDs fabricated based on the LED epitaxial structure (with QW) and a GaN template (without QW). The results are summarized in Table 1.1 to show the R/B ratios with enhancement factor, and the modulation bandwidths of the LED samples at 100 mA in injected current. Here, we can see that the R/B ratio and modulation bandwidth of sample II-H-Q are indeed higher, when compared with the corresponding values of sample I-Q. In Table 1.1, the PL decay times in TRPL study are also shown. In the samples fabricated on GaN template, the QD PL decay time of sample H-Q is indeed shorter than that of sample Q, indicating the higher radiative recombination rate in sample H-Q since the non-radiative recombination rate is fixed. In the sample fabricated on the LED epitaxial structure, the QD (QW) PL decay time becomes longer (shorter) in sample H-Q, when compared with sample Q. These results are attributed to the FRET from QW into QD in the structure with QW. The FRET is enhanced through the nanoscale-cavity effect.

doi:10.6342/NTU202203112

1.5 Research motivations

The study results shown in section 1.3 illustrate the nanoscale-cavity effect of a surface nano-hole on the behaviors of QD emission and FRET. Although certain nanoscale-cavity effects have been observed, many details are still unclear, particularly the basic optical behaviors of the QDs inserted into a nano-hole deserves further investigation. Also, the SP coupling effects caused by the metal NPs inserted into a surface nano-hole have not been studied. The SP coupling process can further enhance the emission and FRET of the QDs inserted into a nano-hole. Such fundamental knowledge about the emission and FRET behavior is important for further improving the design of a color conversion device. In the study of this thesis, we first insert the photoresist solution of green-emitting QDs (GQDs) and red-emitting QDs (RQDs) into the fabricated surface nano-holes on a GaN template for studying the emission behaviors of those QDs and the FRET behavior from GQD into RQD. Chemically synthesized Ag NPs are also immersed into the photoresist for inserting into the nano-hole for producing an SP coupling effect. Then, similar samples are fabricated on an InGaN/GaN QW template, in which nano-holes penetrate through the QW structure such that the QD and Ag NP immersed photoresist contacts the QWs. In this situation, we can study the nanoscale-cavity effect on the FRET from the QWs into the inserted QDs. Finally, shallow nano-holes are fabricated on the QW template such that the bottom of the nano-holes is close to the top QW. By inserting the photoresist solution of QDs into the shallow nano-holes and placing Ag NPs on the sample surface, we can produce the SP coupling between the surface Ag NPs and the QWs. In this situation, the QDs are located between the Ag NPs and QWs for absorbing the strong near-field energy in the SP coupling process. It is expected that the color conversion through the QDs can be enhanced.

doi:10.6342/NTU202203112

1.6 Thesis structure

In Chapter 2 of this thesis, the sample structures and their fabrication procedures are described. Then, the emission, FRET, and SP coupling behaviors of QDs in a surface nano-hole array fabricated on a GaN template are illustrated in Chapter 3. Next, the similar behaviors in a surface nano-hole array fabricated on a QW template are presented in Chapter 4. In Chapter 5, we show the color conversion results of QDs affected by the SP coupling between surface Ag NPs and QWs. Further discussions about the results are made in Chapter 6. Finally, conclusions are drawn in Chapter 7.

doi:10.6342/NTU202203112

Table 1.1 Key data of LED performances and TRPL measurements.

sample	I-Q	II-H-Q
Normalized EL intensity of LED at 100 mA	0.730	0.765 (5 %)
R/B intensity ratio of LED at 100 mA	4.85	5.34 (10 %)
LED Modulation bandwidth at 100 mA (MHz) (blue/red/mixed)	17.75/4.73/5.76	24.24/5.26/7.26
QW PL decay time on LED structure (ns)	132.00	58.16
QD PL decay time on LED structure (ns)	11.21	19.43
QD PL decay time on u-GaN template (ns)	12.42	7.19

doi:10.6342/NTU202203112

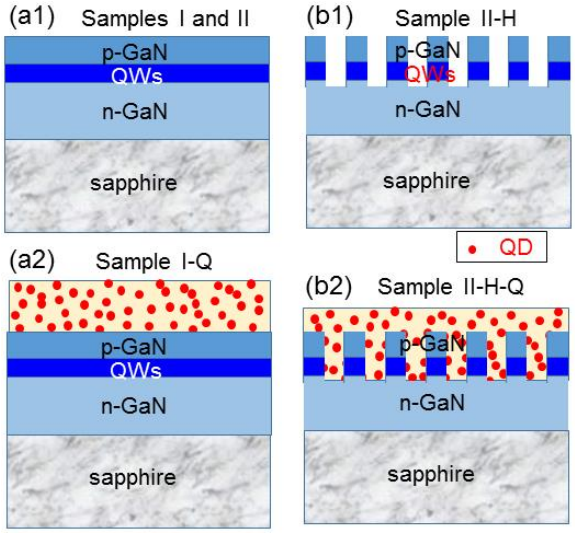

Fig. 1.1 Schematic illustrations of sample structures.

doi:10.6342/NTU202203112

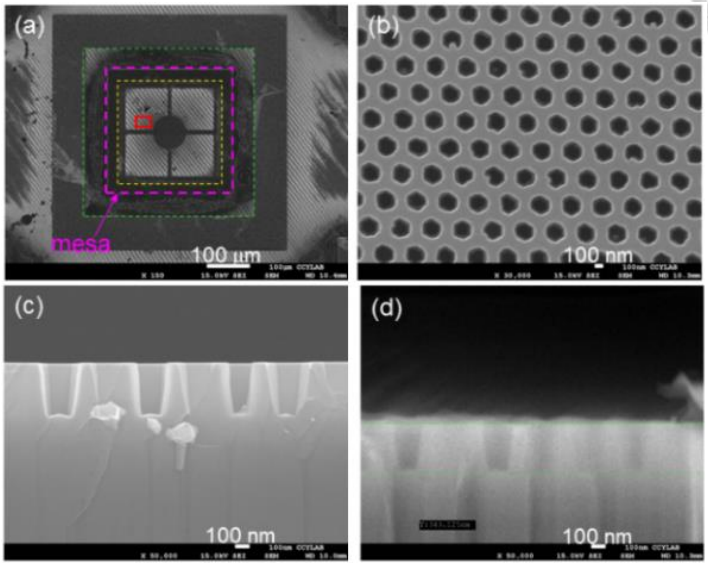

Fig. 1.2 Plane and cross-sectional SEM images of sample II-H.

doi:10.6342/NTU202203112

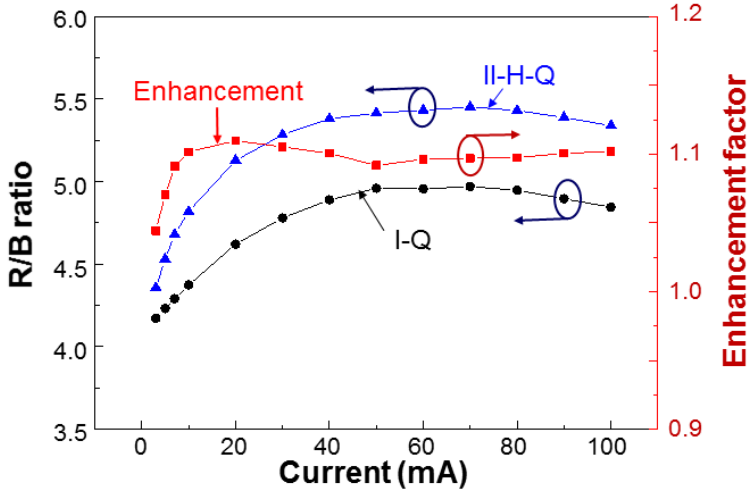

Fig. 1.3 R/B ratio and the enhancement factor.

doi:10.6342/NTU202203112

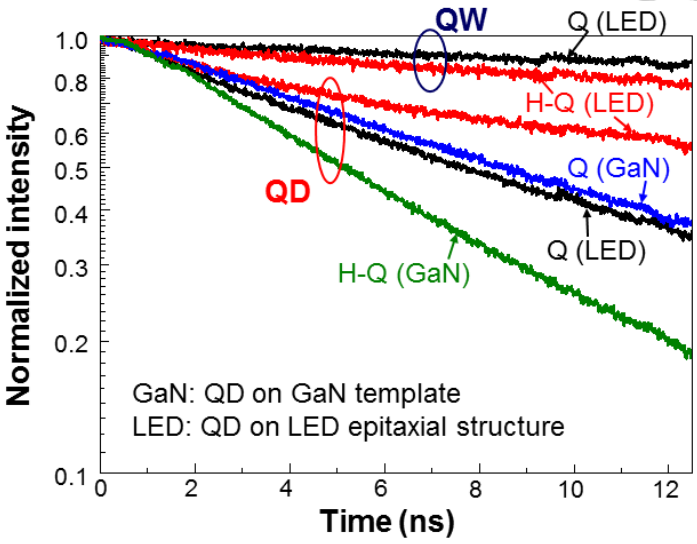

Fig. 1.4 PL decay profiles of the QW and QD emissions.

doi:10.6342/NTU202203112

Chapter 2 Sample Structures and Fabrication Procedures

2.1 Sample structures

Figure 2.1(a) schematically illustrates the structure of the GaN template used for fabricating nano-hole samples without QW. The GaN template is grown with metalorganic chemical vapor deposition (MOCVD) on double-polished sapphire substrate at 1040 ^{o}C. Figure 2.2(a) schematically illustrates the structure of the QW template used for fabricating nano-hole samples with 5 periods of InGaN/GaN QW. On a GaN template, the InGaN well layers and GaN barrier layers are grown at 695 and 793 ^{o}C, respectively. The QW structure is capped by an un-doped GaN (u-GaN) layer of ~50 nm in thickness. The emission wavelength of the QW structure is around 455 nm. On either GaN or QW template, a nano-hole array is fabricated, as schematically illustrated in Figs. 2.1(b) and 2.2(b). On the QW template, the nano-holes are deep enough to penetrate through the QW layer. Photoresist solutions of green-emitting QD (GQD), red-emitting QD (RQD), and/or synthesized Ag nanoparticles (NPs) are inserted into the nano-holes to form various nano-hole samples. For comparison, those photoresist solutions are also placed on the flat top surfaces of the GaN and QW templates to form planar sample, as schematically illustrated in Figs. 2.1(c) and 2.2(c). Two types of Ag NP are synthesized for producing localized surface plasmon (LSP) resonances at different wavelengths. The Ag NP with LSP feature close to the emission wavelength of GQD (RQD) is denoted by GNP (RNP). On GaN templates with surface nano-hole arrays, the combination of QDs and Ag NPs leads to the samples of GN-H-XXX, with XXX = GQD, RQD, GQD+RQD, GQD+GNP, RQD+RNP, GQD+RQD+GNP, and GQD+RQD+RNP. For comparison, the planar samples on GaN templates include GN-R-XXX, with XXX = GQD, RQD, GQD+RQD, GQD+GNP, RQD+RNP, GQD+RQD+GNP, and GQD+RQD+RNP. Similarly, on the QW template, we prepare the nano-hole samples of QW-H-XXX and planar samples of QW-R-XXX.

doi:10.6342/NTU202203112

Besides the comparisons between the QW- and GN- sample series, we also study the QD emission behavior when it is affected by the SP coupling between the QWs and surface Ag NPs. For this study, we fabricate shallow nano-holes in the GaN capping layer on a QW template. The nano-hole bottom is above the top QW. Then, GQD and/or RQD is inserted into the nano-holes, as schematically illustrated in Fig. 2.3(a). This series of sample are denoted by QW-S-XXX, with XXX = GQD, RQD, and GQD+RQD. The SP coupling effect is induced by surface Ag NPs, as schematically illustrated in Fig. 2.3(b). This series of sample are denoted by QW-S-XXX-SP, with XXX = GQD, RQD, and GQD+RQD. The prepared samples in this study (20 samples in total) are summarized in Tables 2.1 and 2.2.

The structure of the QW template is analyzed with cross-sectional transmission electron microscopy (TEM). Figure 2.4 shows a dark-field TEM image of the QW template, in which we can see five periods of QW with the well layer thickness between 2.5 and 2.9 nm and the barrier thickness around 17 nm. Including the top quantum barrier, the capping layer thickness, i.e., the distance between the top QW and sample surface, is around 50 nm. Also, the distance between the bottom QW and sample surface is around 134 nm. Therefore, if we fabricate nano-holes of >300 nm in depth, the QWs can expose on the nano-hole sidewalls, as illustrated in Fig. 2.2(b). On the other hand, for fabricating the samples illustrated in Fig. 2.3(a), the nano-hole depth needs to be smaller than 50 nm.

2.2 Fabrication of a surface nano-hole array

The procedures for fabricating surface nano-hole arrays based on the nano-imprint technique are schematically illustrated in Figs. 2.5(a) through 2.5(f). As shown in Fig. 2.5(a), a SiO_2 layer and a photoresist layer are first coated onto the sample. Then, as illustrated in Fig. 2.5(b), a nano-imprint stamp is used to press the sample to form a triangular nano-hole array on the photoresist layer of 180

doi:10.6342/NTU202203112

nm in hole diameter and 380 nm in hole spacing (center-to-center). Next, we use reactive ion etching (RIE) technique to etch the photoresist and SiO_2 to form a hole array on the two layers, as illustrated in Fig. 2.5(c). This RIE process uses O_2 plasma as etchants for 5 min to etch the photoresist and ChF_3 plasma as etchant for 3 min to etch SiO_2. The photoresist is then removed also with RIE (O_2 plasma as etchant for 20 min), as shown in Fig. 2.5(d). The remaining SiO_2 pattern is used as the mask to etch the p-type and QW structures in the LED sample with inductively coupled plasma RIE (ICP-RIE) and wet etching (with AZ400K), as illustrated in Fig. 2.5(e). In the ICP-RIE process, Cl_2 and Ar are used as plasma etchants for 60 (20) sec to fabricate deep (shallow) nano-holes. Also, the AZ400K wet etching lasts for 7 min at the temperature of 80 ^oC. The wet etching process can help in making the hole sidewall vertical and removing the damaged material on the sidewall. Finally, buffered oxide etchant (BOE) dipping for 1 min at room temperature is undertaken for removing the SiO_2 mask to give us an LED sample with a surface deep nano-hole pattern, as illustrated in Fig. 2.5(f). Figures 2.6(a) and 2.6(b) show the SEM images of a nano-hole array with different magnifications. Although the hole pattern of the nano-imprint stamp is circular, the planar nano-hole pattern is hexagonal. The surface hole size between two parallel sides is ~238 nm. Figures 2.7(a) and 2.7(b) show two cross-sectional SEM images of a nano-hole array in a GaN template. Here, we can see that the nano-hole depth is around 300 nm, which is significantly larger than the depth of the bottom QW when such a nano-hole array is fabricated on a QW template. Here, we can also see that the nano-hole cross-sectional size slightly decreases with depth.

2.3 Colloidal quantum dots and synthesized Ag nanoparticles

The used CdZnSeS/ZnS GQDs and RQDs are purchased from Taiwan Nanocrystals Inc. Hsinchu, Taiwan. They are capped with an amphiphilic polymer, i.e., poly(isobutylene-alt-maleic anhydride),

doi:10.6342/NTU202203112

and hence are negatively charged with zeta potentials at -28.3 and -25.6 mV, respectively [33]. The emission peak wavelengths of GQD and RQD are 530 and 625 nm, respectively. The amphiphilic polymer capped GQD or RQD is a sphere-like particle of 8-10 nm in size. To immerse QDs in the photoresist, which is SU-8, the water solvent of QDs is replaced first by ethanol and then by propylene glycol methyl ether acetate (PGMEA) through centrifugations [34, 35]. QDs can be uniformly dispersed in a PGMEA solution after sonication. For forming the photoresist solution with QDs, we mix 50-mL PGMEA solution of QDs with 380-mg photoresist of SU-8 and stir the mixer through sonication. The QD concentration in the photoresist solution is estimated to be 5 wt%. To deposit an SU-8 solution onto a sample, a drop of the SU-8 solution of ~30 μL in volume is applied to the sample, followed by a spin process of 300 rpm for 30 sec. Then, the sample is baked first at 65 ^{o}C for 20 min and then at 95 ^{o}C for 40 min. Next, we bake the sample again first at 65 ^{o}C for 1 min and then at 95 ^{o}C for 4 min.

Two types of synthesized Ag NPs (GNP and RNP) are fabricated [10, 11, 36]. Figures 2.8(a1) and 2.8(a2) [2.8(b1) and 2.8(b2)] show the SEM images of samples GNP (RNP) with different magnifications when they are placed on GaN templates and dried up. We can see that the shape of the Ag NPs is irregular and the size is not uniform. The average size of RNPs looks larger than that of GNPs. Figure 2.9 shows the normalized extinction spectra of GNP and RNP in water under the conditions before (bare) and after linking with 5 k polyethylene glycol (thiol-PEG-amine) (PEG) [37]. The linkage of PEG can prevent the aggregation of the Ag NPs in a solution. It can also turn the surface charge of an Ag NP into positive such that it can attract negatively charged QDs. Before PEG linkage, the extinction peaks, i.e., LSP resonance peaks, of GNP and RNP are located at 456 and 537 nm, respectively. After PEG linkage, they are red-shifted to 469 and 555 nm, respectively. It is expected that the LSP resonance peaks will be further red-shifted after they are immersed in the

doi:10.6342/NTU202203112

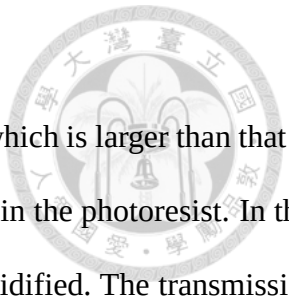

photoresist, SU-8, because the refractive index of the photoresist is 1.577, which is larger than that of water (1.33). Figure 2.10 shows the transmission spectra of GNP and RNP in the photoresist. In this measurement, the photoresist solution is placed on a GaN template and solidified. The transmission spectra in Fig. 2.10 are obtained using the transmission of a pure photoresist (no Ag NP) on a GaN template as measurement baseline. Here, the spectral depressions correspond to the LSP resonance features. We can see that the LSP resonance peak of GNP (RNP) in solidified photoresist is 506 (608) nm. In Fig. 2.10, the two vertical dashed lines indicate the emission wavelengths of GQD and RQD at 530 and 625 nm, respectively. One can see that the LSP resonance peak of GNP (RNP) is close to the emission wavelength of GQD (RQD). In other words, the LSP resonance of GNP (RNP) at the GQD (RQD) emission wavelength is quite strong. In particular, at the GQD (RQD) emission wavelength, the LSP resonance of GNP is stronger (weaker) than that of RNP. Therefore, the SP coupling effects of GNP and RNP can be differentiated.

In inserting the photoresist solution of QD/AG NP into the fabricated nano-holes, a drop of the photoresist solution is applied to the sample surface. After a spin process, the photoresist solution with immersed QDs and/or Ag NPs can flow into the nano-holes. However, since our study targets are the QDs and/or Ag NPs in the nano-holes, the photoresist containing QDs/Ag NPs remains on the sample top surface must be removed. Figure 2.11(a1) shows the SEM image near the edge of a sample, where the photoresist coverage thickness tapers off. The lower dark region corresponds to a thicker coverage, where the photoresist solution exists on the top surface. Because the photoresist solution is electric insulating, it looks dark in SEM observation. The upper brighter region in Fig. 2.11(a1) corresponds to a thinner coverage, where all the photoresist solution flows into the nano-holes. Figures 2.11(a2) and 2.11(a3) show the magnified SEM images at the boundary in Fig. 2.11(a1). We can see the inserted photoresist solution in the nano-holes. To remove the remained photoresist

doi:10.6342/NTU202203112

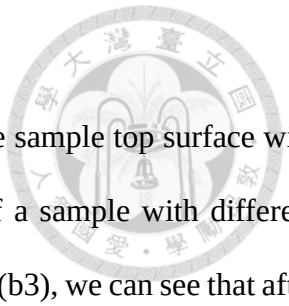

solution on the sample top surface, i.e., clean sample surface, we sweep the sample top surface with a wet cotton swab. Figures 2.11(b1)-2.11(b3) show three SEM images of a sample with different magnifications after surface cleaning. By comparing Figs. 2.11(a3) and 2.11(b3), we can see that after surface cleaning, the photoresist solution in the shallow region around a nano-hole is removed. However, that inside the nano-holes remains.

2.4 Optical characterization methods

To understand the emission and FRET behaviors of QDs and QWs, the time-resolved (TR) PL and continuous (cw) PL spectroscopy measurements are undertaken. TRPL measurement is excited by the second-harmonic (390 nm in wavelength and ~1.5 mW in power) of a femtosecond Ti:sapphire laser (Coherent, VERDI-8W). The signals are monitored with a photon counter of 2.5 ps in temporal resolution (Acton research Corporation, SpectraPro 2150i). The measurement of cw PL is excited by an InGaN laser diode of 405 nm in wavelength and 6 mW in output. The spectroscopic signals are detected by an Ocean Optics spectrometer. Only room-temperature measurement is undertaken. In both TRPL and cw PL measurements, the excitation lasers are incident onto the sample from the sapphire side. The emitted PL signals are also collected from the sapphire side.

doi:10.6342/NTU202203112

Table 2.1 List of the samples based on the GaN and QW templates and their descriptions. PR: photoresist.

Samples on GaN template	Samples on QW template	Description
GN-H-GQD	QW-H-GQD	PR containing GQD in deep nano-holes
GN-H-RQD	QW-H-RQD	PR containing RQD in deep nano-holes
GN-H-GQD+RQD	QW-H-GQD+RQD	PR containing GQD & RQD in deep nano-holes
GN-H-GQD+GNP	QW-H-GQD+GNP	PR containing GQD & GNP in deep nano-holes
GN-H-RQD+RNP	QW-H-RQD+RNP	PR containing RQD & RNP in deep nano-holes
GN-H-GQD+RQD+GNP	QW-H-GQD+RQD+GNP	PR containing GQD, RQD & GNP in deep nano-holes
GN-H-GQD+RQD+RNP	QW-H-GQD+RQD+RNP	PR containing GQD, RQD & RNP in deep nano-holes
GN-R-GQD	QW-R-GQD	PR containing GQD on surface
GN-R-RQD	QW-R-RQD	PR containing RQD on surface
GN-R-GQD+RQD	QW-R-GQD+RQD	PR containing GQD & RQD on surface
GN-R-GQD+GNP	QW-R-GQD+GNP	PR containing GQD & GNP on surface
GN-R-RQD+RNP	QW-R-RQD+RNP	PR containing RQD & RNP on surface
GN-R-GQD+RQD+GNP	QW-R-GQD+RQD+GNP	PR containing GQD, RQD & GNP on surface
GN-R-GQD+RQD+RNP	QW-R-GQD+RQD+RNP	PR containing GQD, RQD & RNP on surface

doi:10.6342/NTU202203112

Table 2.2 List of the samples for studying the SP coupling. PR: photoresist.

Sample	Description
QW-S-GQD	PR containing GQD in shallow nano-holes
QW-S-RQD	PR containing RQD in shallow nano-holes
QW-S-GQD+RQD	PR containing GQD & RQD in shallow nano-holes
QW-S-GQD-SP	PR containing GQD in shallow nano-holes overlaid with surface Ag NPs
QW-S-RQD-SP	PR containing RQD in shallow nano-holes overlaid with surface Ag NPs
QW-S-GQD+RQD-SP	PR containing GQD & RQD in shallow nano-holes overlaid with surface Ag NPs

doi:10.6342/NTU202203112

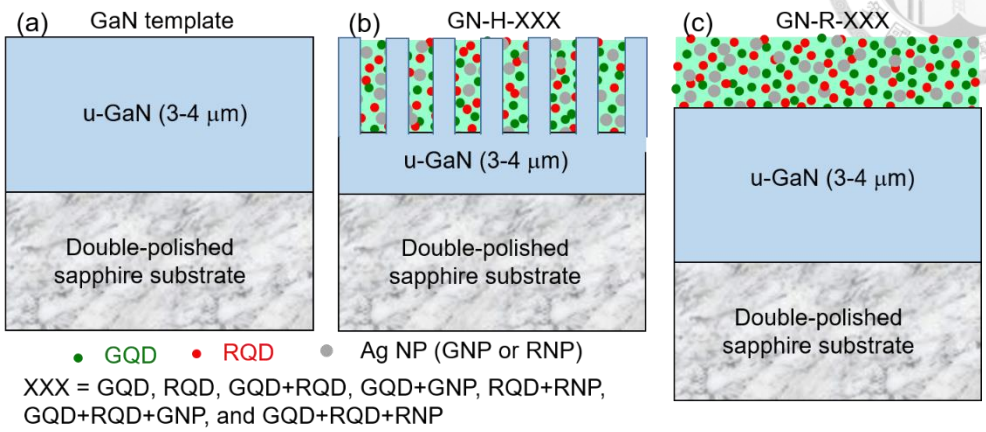

Fig. 2.1 (a): Schematic illustration of the structure of the GaN template. (b): Schematic illustration of the structures of samples GN-H-XXX with QDs and/or Ag NPs in deep nano-holes. (c): Schematic illustration of the structures of samples GN-R-XXX with QDs and/or Ag NPs on the sample surface.

doi:10.6342/NTU202203112

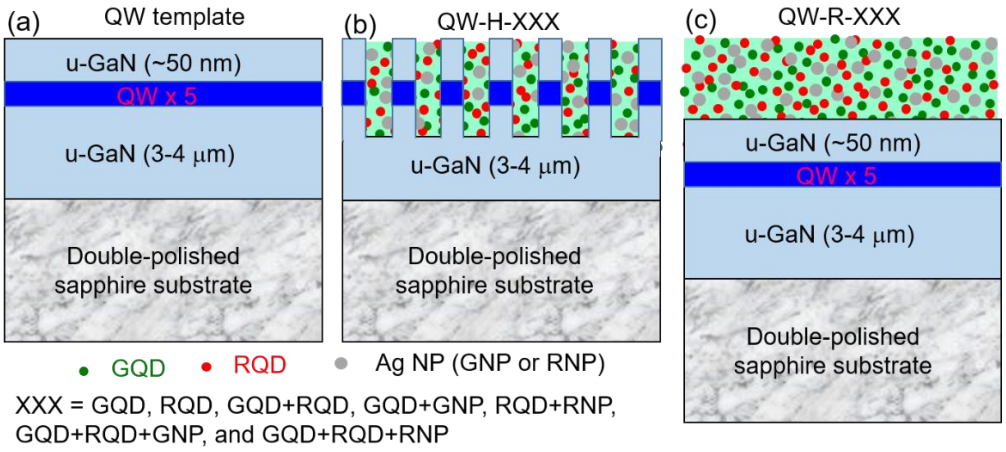

Fig. 2.2 (a): Schematic illustration of the structure of the QW template. (b): Schematic illustration of the structures of samples QW-H-XXX with QDs and/or Ag NPs in deep nano-holes. (c): Schematic illustration of the structures of samples QW-R-XXX with QDs and/or Ag NPs on the sample surface.

doi:10.6342/NTU202203112

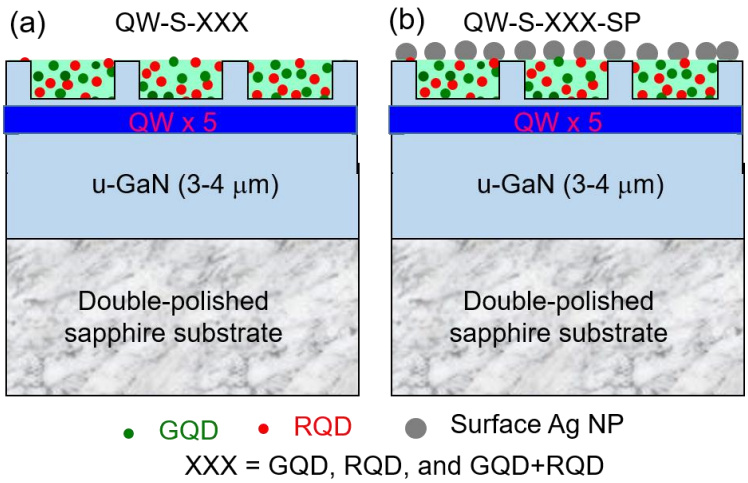

Fig. 2.3 (a): Schematic illustration of the structures of samples QW-S-XXX with QDs in shallow nano-holes. (b): Schematic illustration of the structures of samples QW-S-XXX-SP with QDs in shallow nano-holes and Ag NPs on the top surface.

doi:10.6342/NTU202203112

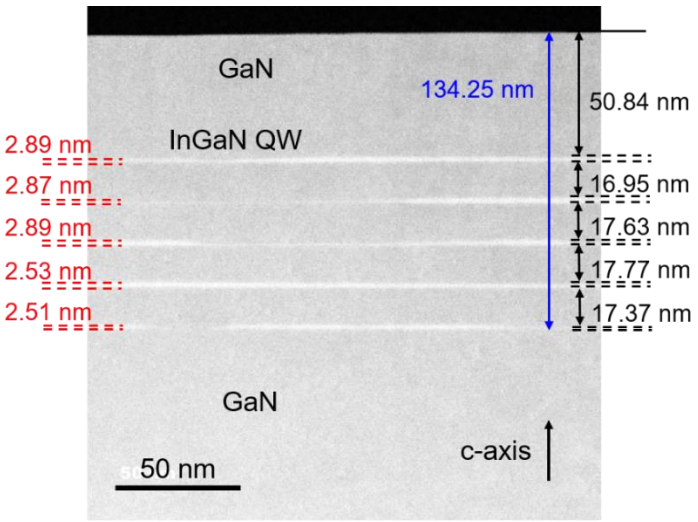

Fig. 2.4 Cross-sectional TEM image of the QW template showing the QW structure.

doi:10.6342/NTU202203112

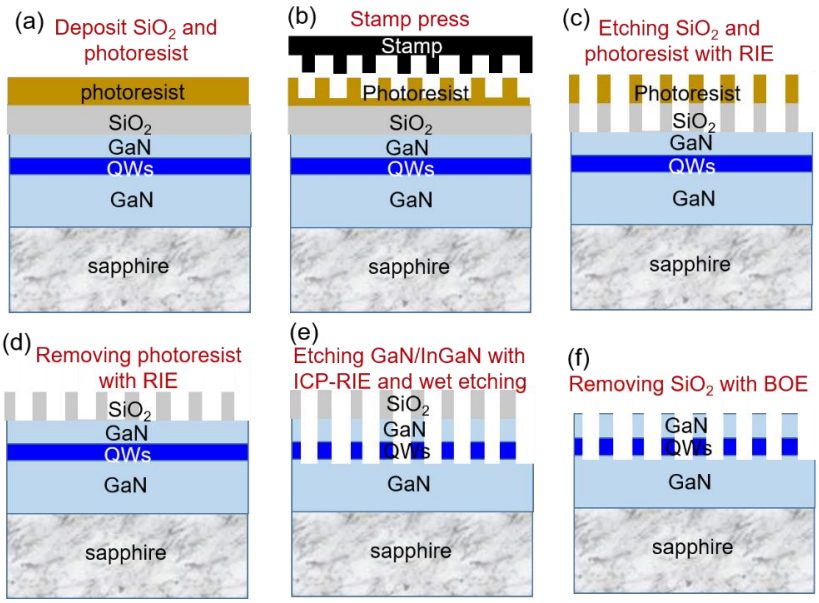

Fig. 2.5 (a)-(f): Schematic illustrations of the surface nano-hole fabrication procedures.

doi:10.6342/NTU202203112

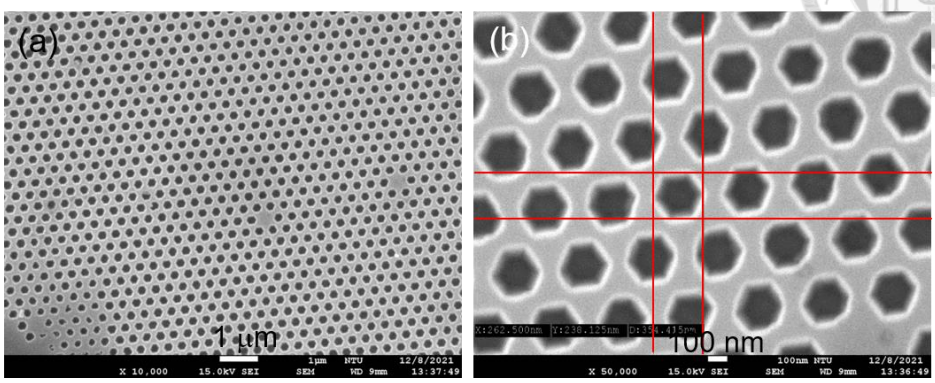

Fig. 2.6 (a) and (b): Plane-view SEM images of a fabricated surface nano-hole array with different magnifications.

doi:10.6342/NTU202203112

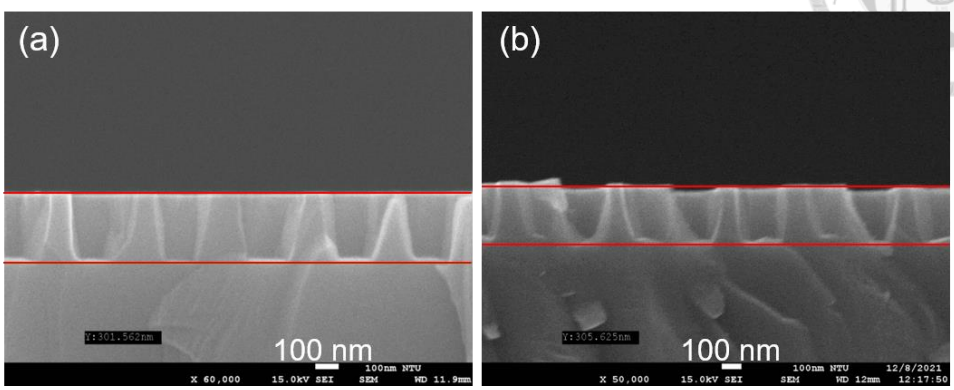

Fig. 2.7 (a) and (b): Cross-sectional SEM images of a fabricated surface nano-hole array at different locations.

doi:10.6342/NTU202203112

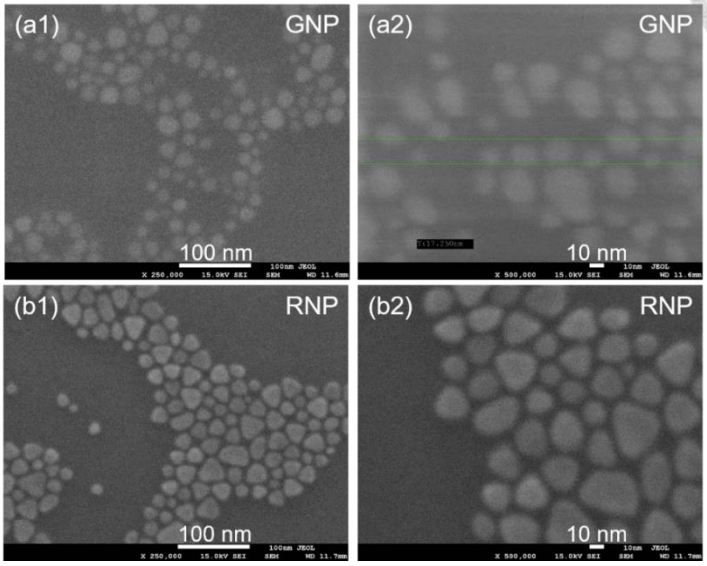

Fig. 2.8 (a1) and (a2) [(b1) and (b2)]: SEM images of dried GNPs (RNPs) on GaN templates with different magnifications.

doi:10.6342/NTU202203112

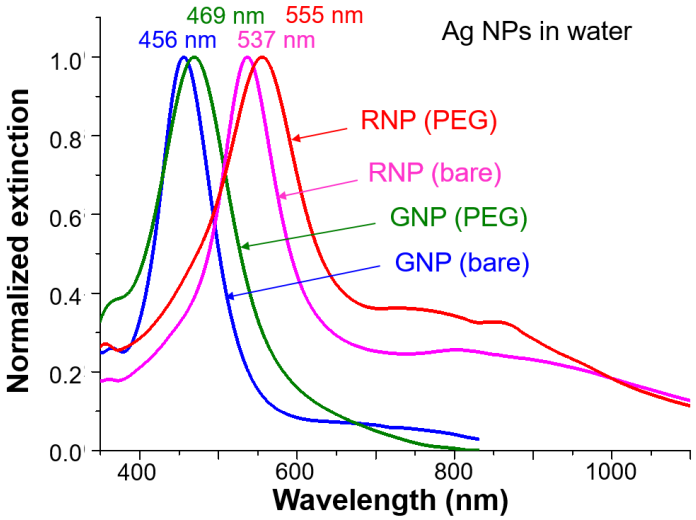

Fig. 2.9 Normalized extinction spectra of GNP and RNP in water before (bare) and after PEG linkage (PEG). The numbers indicate the spectral peak wavelengths.

doi:10.6342/NTU202203112

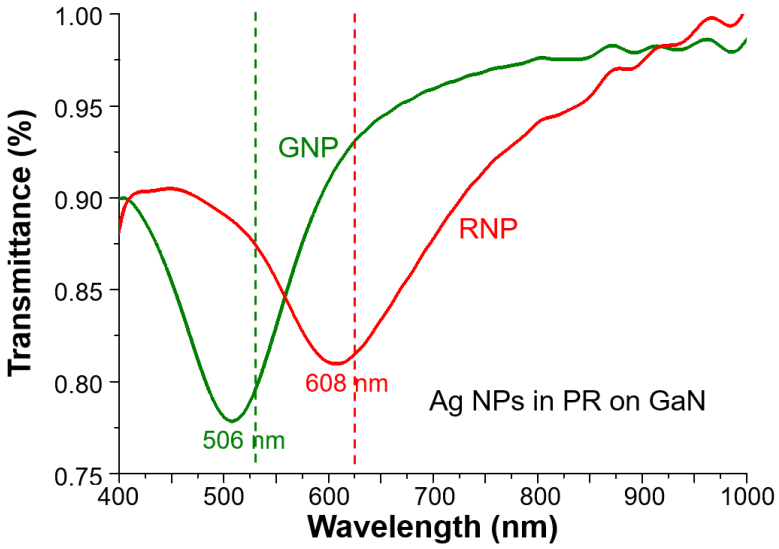

Fig. 2.10 Transmission spectra of GNP and RNP in solidified photoresist placed on GaN templates. The numbers show the minima wavelengths.

doi:10.6342/NTU202203112

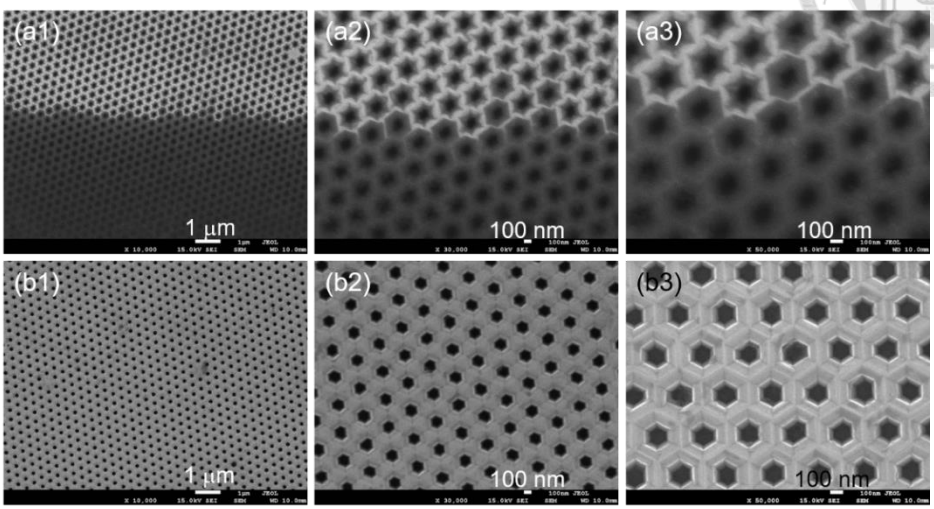

Fig. 2.11 (a1)-(a3): SEM images of different magnifications of a nano-hole array covered by the photoresist solution (before surface cleaning). (b1)-(b3): SEM images of different magnifications of a nano-hole array with the photoresist solution inserted into the nano-holes (aftere surface cleaning).

doi:10.6342/NTU202203112

Chapter 3 Emission, Förster Resonance Energy Transfer and Surface Plasmon Coupling in a Surface Nanoscale Hole on a GaN Template

3.1 Time-resolved photoluminescence results

Figure 3.1 shows the green-light PL decay profiles of samples GN-R-GQD, GN-R-GQD+RQD, GN-R-GQD+GNP, GN-R-GQD+RQD+GNP, and GN-R-GQD+RQD+RNP. Here, one can see that the green-light decay rate increases when RQD is added to produce FRET or Ag NP is added to produce SP coupling. Figure 3.2 shows the red-light PL decay profiles of samples GN-R-RQD, GN-R-GQD+RQD, GN-R-RQD+RNP, GN-R-GQD+RQD+GNP, and GN-R-GQD+RQD+RNP. Here, when GQD is added to produce FRET, the red-light PL decay rate is reduced. When GNP or RNP is added for producing SP coupling, the red-light PL decay rate is increased. Figure 3.3 shows the green-light PL decay profiles of samples GN-H-GQD, GN-H-GQD+RQD, GN-H-GQD+GNP, GN-H-GQD+RQD+GNP, and GN-H-GQD+RQD+RNP. The general variation trend of those curves is the same as that in Fig. 3.1. For comparison, the green-light PL decay profile of sample GN-H-GQD+RQD before surface cleaning is also shown. We can see that under this condition, the green-light decay rate is lower than that after surface cleaning. Figure 3.4 shows the red-light PL decay profiles of samples GN-H-RQD, GN-H-GQD+RQD, GN-H-RQD+RNP, GN-H-GQD+RQD+GNP, and GN-H-GQD+RQD+RNP. Generally, the variation trend of those decay profiles is the same as that in Fig. 3.2. Again, for comparison, the red-light PL decay profile of sample GN-H-GQD+RQD before surface cleaning is also shown in Fig. 3.4. We can see that under this condition, the red-light decay rate is lower than that after surface cleaning.

In Table 3.1, we show the green- and red-light PL decay times of the samples fabricated on the GaN template. In sample GN-R-GQD (GN-R-RQD), the green-light (red-light) PL decay times is

doi:10.6342/NTU202203112

6.24 (8.65) ns. This number represents the GQD (RQD) PL decay behavior in the solidified photoresist on the sample surface. The decay time of GQD emission decreases from 6.24 ns to 5.81 ns when GQDs are inserted into the deep nano-holes in sample GN-H-GQD. This result is attributed to the nanoscale-cavity effect, which enhances the emission efficiency of a QD and hence reduces the PL decay time. A similar result can be observed for RQD. The decay time of GQD emission decreases from 8.65 ns to 7.27 ns when RQDs are inserted into the deep nano-holes in sample GN-H-RQD. When GQD is linked with GNP for producing SP coupling in sample GN-R-GQD+GNP, the green-light PL decay time is reduced from 6.24 ns to 5.51 ns because the SP coupling can also enhance the GQD emission efficiency and hence reduce its decay time. Again, the similar behavior can be observed for RQD in sample GN-R-RQD+RNP. The red-light decay time reduces from 8.65 ns to 7.79 ns. When GQD+GNP (RQD+RNP) is inserted into a nano-hole, the decay time of GQD (RQD) is further reduced to 4.63 (6.91) ns, indicating that the SP coupling is stronger in a nanoscale cavity.

When both GQD and RQD exist in sample GN-R-GQD+RQD, FRET from GQD into RQD occurs such that the green-light decay time is reduced from 6.24 ns to 4.98 ns and red-light decay time is increased from 8.65 ns to 10.47 ns on the sample surface. When GQD and RQD are inserted into a nano-hole, as the case of sample GN-H-GQD+RQD, two competing factors counteract in determining the emission behavior. The nanoscale-cavity effect can enhance the FRET process to further reduce (increase) green-light (red-light) decay time. However, the nanoscale-cavity effect can also enhance the QD emission efficiency such that both green- and red-light decay times are reduced. The additive effect leads to a further reduction of GQD PL decay time (from 4.98 ns to 4.09 ns). However, the subtractive effect results in a decrease of RQD PL decay time (10.47 ns to 8.62 ns). The underlined numbers in Table 3.1 show the decay times of sample GN-H-GQD+RQD before surface cleaning. In this situation, we can see that either green- or red-light decay time lies between those of

doi:10.6342/NTU202203112

samples GN-R-GQD+RQD and GN-H-GQD+RQD (after surface cleaning). The results of sample GN-H-GQD+RQD before surface cleaning are actually closer to those of sample GN-R-GQD+RQD, confirming that the density of the QDs remaining on the sample top surface is higher than that inserted into the nano-holes and hence dominates the PL decay behavior.

Next, when GNP or RNP is added to the GQD+RQD system, the FRET behavior can be affected by SP coupling. In sample GN-R-GQD+RQD+GNP, the green-light decay time is further reduced to 4.50 ns (from 4.98 ns in sample GN-R-GQD+RQD). However, this reduction is not necessarily caused by enhanced FRET. It can be due to the SP-coupling enhanced GQD emission. In this sample, the red-light decay time is reduced to 9.77 ns (from 10.47 ns in sample GN-R-GQD+RQD), confirming that the SP coupling also enhances RQD emission, but not necessarily enhance FRET. In sample GN-H-GQD+RQD+GNP, both green- and red-light decay times are further reduced due to the enhanced QD emission efficiency caused by the nanoscale-cavity effect. Nevertheless, the FRET efficiency in the nano-hole can be enhanced. When RNP is used, instead of GNP, in samples GN-R-GQD+RQD-RNP and GN-H-GQD+RQD-RNP, all the decay times are further reduced. Here, the further reduction of red-light decay times are due to the stronger SP coupling of RNP at the wavelength of RQD emission. The further reduction of green-light decay times can be attributed to the enhanced FRET in this case. With the enhanced carrier decay rate in RQD, the energy transfer from GQD into RQD can become more effective.

The numbers inside the curly brackets show the FRET efficiencies in some of the samples. The FRET efficiency is defined as $\eta = 1-\tau_{DA}/\tau_D$. Here, τ_{DA} (τ_D) is the PL decay time of donor in the presence (absence) of acceptor. In Table 3, we can see that the FRET efficiency is always higher when QDs are inserted into a nano-hole. With the SP coupling of GNP, in either case of surface QDs or QDs in a nano-hole, FRET efficiency is reduced, indicating that this SP coupling leads to a reduction

doi:10.6342/NTU202203112

of FRET efficiency.

3.2 Continuous photoluminescence results

Figure 3.5 shows the normalized spectra of those samples with both GQD and RQD, including sample GN-H-GQD+RQD before surface cleaning. All the spectra are normalized with respect to the individual peak intensities of green light. The ratio (R/G ratio) of the integrated intensity of red light over that of green light for each of those samples is shown inside the parentheses in Table 3.1. In the sample series of surface QDs (nano-hole QDs), the R/B ratio decreases from 4.94 (6.26) in sample GN-R-GQD+RQD (GN-H-GQD+RQD) to 4.43 (5.30) in sample GN-R-GQD+RQD+GNP (GN-H-GQD+RQD+GNP), and then increases to 5.67 (6.81) in sample GN-R-GQD+RQD+RNP (GN-H-GQD+RQD+RNP). We can see that with QDs in the nano-holes, the R/G ratios are always higher than the corresponding values in the case of surface QDs, confirming the enhanced FRET effect in the nano-holes. The R/G ratios are decreased in the samples with GNP because the GNP induced SP coupling leads to a larger enhancement of green-light emission. The R/G ratios are increased in the samples with RNP because the RNP induced SP coupling results in a larger enhancement of red-light emission. The R/G ratio of sample GN-H-GQD+RQD before surface cleaning (5.01) is quite close to that of sample GN-R-GQD+RQD (4.94), indicating that the emission behavior of the whole sample is dominated by surface QDs before surface cleaning.

doi:10.6342/NTU202203112

Table 3.1 PL decay times of various samples. The numbers inside the parentheses show the R/G ratios. The numbers inside the curly brackets show the FRET efficiencies. The underlined numbers show the data of sample GN-H-GQD+RQD before surface cleaning.

XXX =		GN-R-XXX (ns)	GN-H-XXX (ns)
GQD	G	6.24	5.81
RQD	R	8.65	7.27
GQD+GNP	G	5.51	4.63
RQD+RNP	R	7.79	6.91
GQD+RQD	G	4.98 (1) {20.2 %}	4.09 (1)/<u>4.67 (1)</u> {29.6 %}
	R	10.47 (4.94)	8.62 (6.26)/<u>10.42 (5.01)</u>
GQD+RQD+GNP	G	4.50 (1) {18.3 %)	3.61 (1) {22.0 %}
	R	9.77 (4.43)	8.51 (5.30)
GQD+RQD+RNP	G	4.39 (1)	3.39 (1)
	R	9.06 (5.67)	7.50 (6.81)

doi:10.6342/NTU202203112

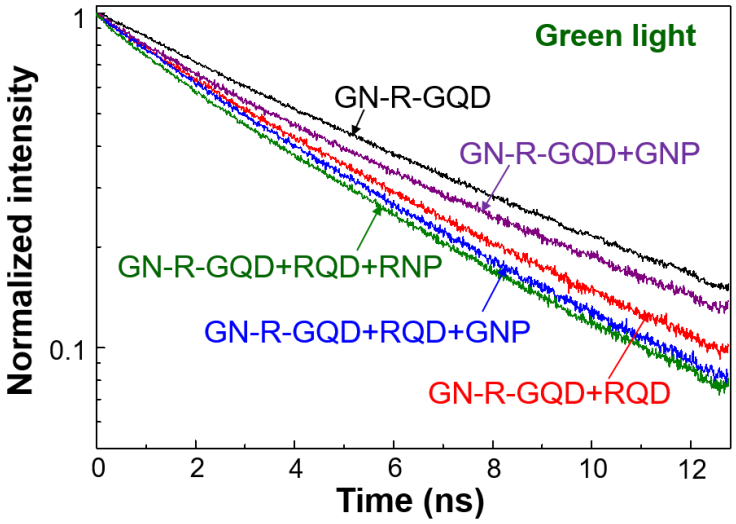

Fig. 3.1 Green-light PL decay profiles of samples GN-R-GQD, GN-R-GQD+RQD, GN-R-GQD+GNP, GN-R-GQD+RQD+GNP, and GN-R-GQD+RQD+RNP.

doi:10.6342/NTU202203112

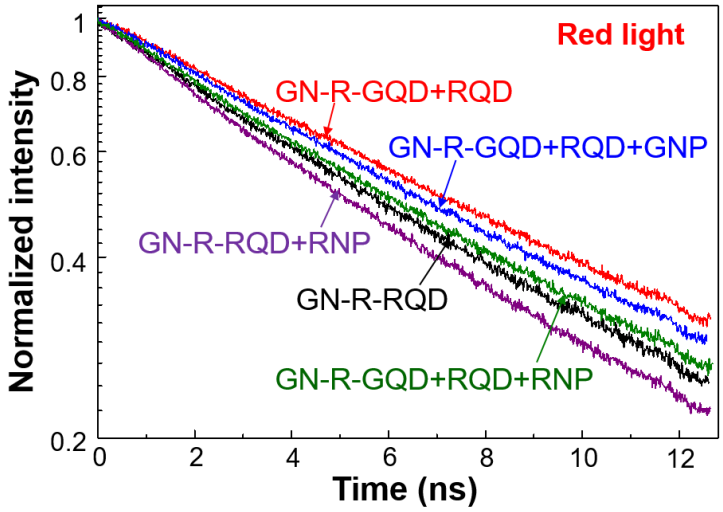

Fig. 3.2 Red-light PL decay profiles of samples GN-R-RQD, GN-R-GQD+RQD, GN-R-RQD+RNP, GN-R-GQD+RQD+GNP, and GN-R-GQD+RQD+RNP.

doi:10.6342/NTU202203112

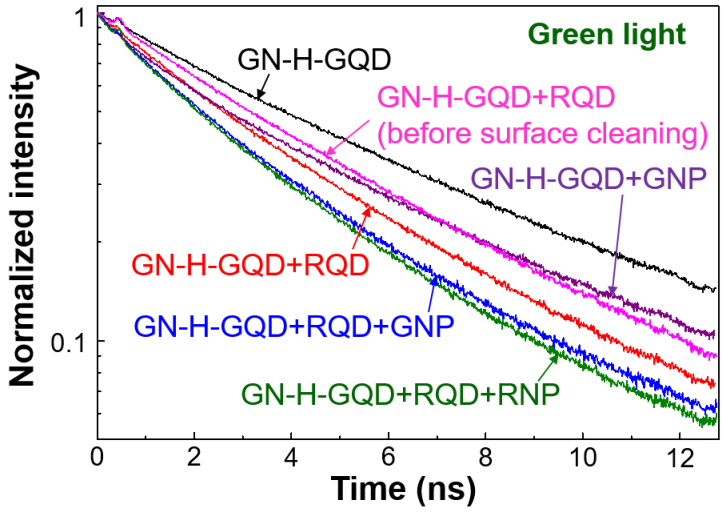

Fig. 3.3 Green-light PL decay profiles of samples GN-H-GQD, GN-H-GQD+RQD, GN-H-GQD+GNP, GN-H-GQD+RQD+GNP, and GN-H-GQD+RQD+RNP. For comparison, the green-light PL decay profile of sample GN-H-GQD+RQD before surface cleaning is also shown.

doi:10.6342/NTU202203112

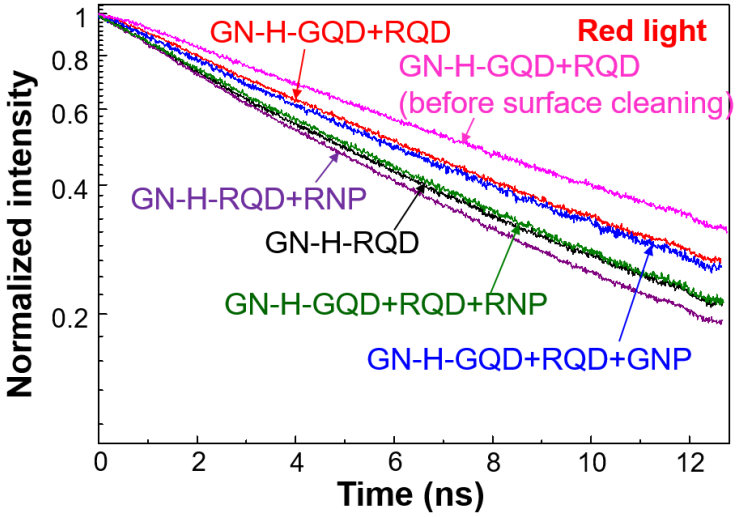

Fig. 3.4 Red-light PL decay profiles of samples GN-H-RQD, GN-H-GQD+RQD, GN-H-RQD+RNP, GN-H-GQD+RQD+GNP, and GN-H-GQD+RQD+RNP. For comparison, the red-light PL decay profile of sample GN-H-GQD+RQD before surface cleaning is also shown.

doi:10.6342/NTU202203112

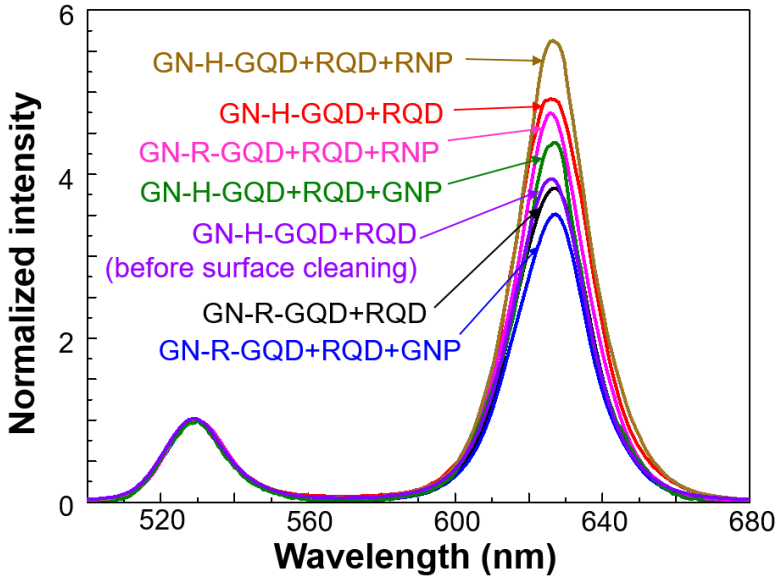

Fig. 3.5 Normalized spectra of samples GN-R-GQD+RQD, GN-R-GQD+RQD+GNP, GN-R-GQD+RQD+RNP, GN-H-GQD+RQD, GN-H-GQD+RQD+GNP, and GN-H-GQD+RQD+RNP. For comparison, that of sample GN-H-GQD+RQD before surface cleaning is also shown.

doi:10.6342/NTU202203112

Chapter 4 Emission, Förster Resonance Energy Transfer and Surface Plasmon Coupling in a Surface Nanoscale Hole on a Quantum-well Structure

4.1 Emission behaviors of quantum-well templates

Although the small pieces of QW samples come from a full 2-inch wafer, because the MOCVD growth of the QW template is not uniform over the wafer, the emission properties of the QWs in those QW samples differ slightly. Therefore, we measure the emission behavior of each QW sample before the application of the photoresist solution. Figures 4.1(a)-4.1(d) show the normalized PL spectra of the QWs in samples QW-R-GQD, QW-R-RQD, QW-R-GQD+RQD, and QW-R-GQD+GNP, respectively. Figures 4.2(a)-4.2(c) show the similar results for samples QW-R-RQD+RNP, QW-R-GQD+RQD+GNP, and QW-R-GQD+RQD+RNP, respectively. The ratio of the integrated intensity at 300 K over that at 10 K is defined as the internal quantum efficiency (IQE). IQEs of those samples are shown in the figures. They range from 50.0 through 52.5 %.

When nano-holes are fabricated on a QW template, the nano-holes can relax the compressive strain in the QW structure such that its quantum-confined Stark effect is reduced. In this situation, the emission efficiency or the IQE of the QW structure can be enhanced. Figures 4.3(a)-4.3(d) show the normalized PL spectra of the QWs in samples QW-H-GQD, QW-H-RQD, QW-H-GQD+RQD, and QW-H-GQD+GNP, respectively, before (B) and after (A) nano-hole fabrication. Figures 4.4(a)-4.4(c) show the similar results for samples QW-H-RQD+RNP, QW-H-GQD+RQD+GNP, and QW-H-GQD+RQD+RNP, respectively. The IQEs before and after nano-hole fabrication are also shown in the figures. We can see that the IQE of the QW structure increases by 8-12 % after nano-holes are fabricated.

doi:10.6342/NTU202203112

4.2 Time-resolved photoluminescence results

Figure 4.5 shows the normalized green-light PL decay profiles of samples QW-R-GQD, QW-R-GQD+GNP, QW-R-GQD+RQD, QW-R-GQD+RQD+GNP, and QW-R-GQD+RQD+RNP. Again, one can see that the green-light decay rate increases when RQD is added to produce FRET or Ag NP is added to produce SP coupling. Figure 4.6 shows the red-light PL decay profiles of samples QW-R-RQD, QW-R-GQD+RQD, QW-R-RQD+RNP, QW-R-GQD+RQD+GNP, and QW-R-GQD+RQD+RNP. Again, when GQD is added to produce FRET, the red-light PL decay rate is reduced. When GNP or RNP is added for producing SP coupling, the red-light PL decay rate is increased. Figure 4.7 shows the green-light PL decay profiles of samples QW-H-GQD, QW-H-GQD+RQD, QW-H-GQD+GNP, QW-H-GQD+RQD+GNP, and QW-H-GQD+RQD+RNP. The general variation trend of those curves is the same as that in Fig. 4.5. For comparison, the green-light PL decay profile of sample QW-H-GQD+RQD before surface cleaning is also shown. We can see that under this condition, the green-light decay rate is lower than that after surface cleaning. Figure 4.8 shows the red-light PL decay profiles of samples QW-H-RQD, QW-H-GQD+RQD, QW-H-RQD+RNP, QW-H-GQD+RQD+GNP, and QW-H-GQD+RQD+RNP. Generally, the variation trend of those decay profiles is the same as that in Fig. 4.6. Again, for comparison, the red-light PL decay profile of sample QW-H-GQD+RQD before surface cleaning is also shown in Fig. 4.8. We can see that under this condition, the red-light decay rate is significantly lower than that after surface cleaning.

Figure 4.9 shows the blue-light PL decay profiles of samples QW-R-GQD and QW-H-GQD under different conditions. For sample QW-R-GQD, the results include the intrinsic condition and that after QD/Ag NP application. For sample QW-H-GQD, the results include the intrinsic condition, that after nano-hole application, and that after QD/Ag NP application and surface cleaning. Here, we can see that after nano-hole application, the PL decay rate is significantly increased in sample QW-

doi:10.6342/NTU202203112

H-GQD. This variation is consistent with the significant increase of QW IQE after nano-hole application. It is noted that this increase of PL decay rate after nano-hole fabrication can have two causes, including the radiative recombination enhancement due to the reduction of the quantum-confined Stark effect and the non-radiative recombination enhancement due to the increase of surface state on a nano-hole sidewall. After QD/Ag NP application, the photoresist filling into the nano-holes can reduce the surface state and hence weaken non-radiative recombination such that the PL decay rate is decreased. In sample QW-R-GQD, the application of QD/Ag NP leads to the increase of PL decay rate because the FRET from QWs into GQDs can speed up carrier decay in the QWs. This FRET effect for enhancing blue-light PL decay also occur in sample QW-H-GQD. However, the PL decay behavior in this situation is dominated by the factor of PL decay weakening due to the reduction of non-radiative recombination. Therefore, in Fig. 4.9, we observe the reduction of PL decay rate after QD/Ag NP application and surface cleaning in sample QW-H-GQD.

Figures 4.10-4.15 show the results for sample sets QW-R-RQD/QW-H-RQD, QW-R-GQD+GNP/QW-H-GQD+GNP, QW-R-RQD+RNP/QW-H-RQD+RNP, QW-R-GQD+RQD/QW-H-GQD+RQD, QW-R-GQD+RQD+GNP/QW-H-GQD+RQD+GNP, and QW-R-GQD+RQD+RNP/QW-H-GQD+RQD+RNP, respectively. The variation trends of the corresponding PL decay profiles are the same among those sample sets. In Fig. 4.13 for sample set QW-R-GQD+RQD/QW-H-GQD+RQD, we also include the result of sample QW-H-GQD+RQD after QD/Ag NP application, but before surface cleaning. This blue-light PL decay profile is quite close to that of the same sample after surface cleaning, indicating that under this condition the FRET from the QWs into the QDs in the nano-holes have almost exhausted the QW carrier such that extra QDs on the sample surface does not produce a stronger FRET effect.

Table 4.1 shows the PL decay times of blue-, green-, and red-light in all the samples based on the

doi:10.6342/NTU202203112

QW template under different conditions. We start the discussions with the green-light decay time of sample QW-R-GQD at 6.43 ns. This number is larger than that in sample GN-R-GQD at 6.24 ns. The larger PL decay time in sample QW-R-GQD is due to the FRET from the QWs into the GQDs on the sample surface. This FRET process can occur even though the GaN capping layer thickness is around 50 nm. This FRET process can also occur in sample QW-R-RQD. Therefore, the red-light decay time of 9.52 ns is longer than that in sample GN-R-RQD at 8.65 ns. When GQD or RQD is inserted into a nano-hole on a QW template in sample QW-H-GQD or QW-H-RQD, as shown in Table 4.1, the PL decay time (5.84 or 7.29 ns) becomes shorter, when compared to the corresponding value of the surface QD sample (6.43 or 9.52 ns). This comparison result implies that the FRET effect from the QWs into the QDs inserted into the nano-holes is not necessarily stronger that that from the QWs into the surface QDs. The behavior of QD PL decay in a nano-hole is dominated by the enhanced QD emission efficiency to reduce its decay time. This speculation is supported by the decay time comparison between the samples fabricated on the GaN and QW templates. The green-light (red-light) decay time of sample QW-H-GQD (QW-H-RQD), i.e., 5.84 ns (7.29 ns), is comparable to that of sample GN-H-GQD (GN-H-RQD), i.e., 5.81 ns (7.27 ns). These comparisons confirm that the FRET from the QWs into QDs in the nano-holes is weak. Therefore, the QD decay time in a nano-hole is only slightly increased on a QW template, when compared to that on a GaN template. It has been reported that the FRET from QWs into the QDs inserted fabricated nano-holes can be significantly stronger than that from QWs into the QDs on the sample surface. This can be true when the QWs are far away the sample surface. However, if we increase the period number of QWs, the FRET from QWs into the QDs inserted fabricated nano-holes can become stronger.

Then, in samples QW-R-GQD+GNP and QW-R-RQD+RNP, their decay times are shorter than the corresponding values in samples QW-R-GQD and QW-R-RQD, respectively, due to the SP

doi:10.6342/NTU202203112

coupling effect for enhancing QD emission efficiency. Those decay times are longer than the corresponding values of samples GN-R-GQD+GNP and GN-R-RQD+RNP, respectively, due to the FRET from QW into QD. In samples QW-H-GQD+GNP and QW-H-RQD+RNP, the decay times are shortened, when compared to the corresponding samples with QDs on the top surface, due to the enhanced emission effect in the nano-holes. With both GQD and RQD in a sample, the green-light decay time is significantly reduced, caused by the FRET from GQD into RQD. In this situation, the red-light decay time can be increased. However, as mentioned earlier, the decay behavior of a QD in a nano-hole is dominated by the emission efficiency enhancement. The generally shorter decay times of GQD and RQD in the nano-holes of the samples with QWs, when compared with those of the samples without QW, are attributed to the stronger nanoscale-cavity effect for enhancing QD emission efficiency. However, the basic mechanism leading to this behavior is still unclear. One of the possible causes is the FRET from inserted QDs into the surface defect states on the nano-hole sidewall. The weak FRET from the QWs into QDs in the nano-holes can be understood by comparing the depth of the nano-hole (~300 nm), the thickness of the QW structure (~75 nm), and the diameter of the nano-hole (~200 nm). The portion of the inserted QDs for effectively interacting with QWs through FRET is small if the QD distribution in the photoresist is essentially uniform.

Table 4.1 also shows the PL decay times of the QWs. In the sample series of QW-R-XXX, the numbers before and after the slash in each box correspond to the decay times before and after QD/PR application. After QD/PR application, the QW decay time is always significantly reduced, indicating the effective FRET from the QWs into the surface QDs. In the sample series of QW-H-XXX, the three numbers separated by the two slashes correspond to the QW decay times before and after nano-hole fabrication, and after QD/PR insertion into the nano-holes. In each sample, after nano-hole fabrication, the QW decay time is significantly reduced. Then after QD/PR insertion, the QW decay

doi:10.6342/NTU202203112

time is slightly recovered. The decay time reduction is due to two causes. First, the fabrication of the nano-hole array can relax the strain and hence increase the QW emission efficiency. The strain relaxation also produce the blue-shift of the emission peak, as shown in Figs. 4.3 and 4.4, particularly at the room temperature. Second, the fabrication of the nano-holes produces surface defect states on the sidewalls. In other words, both radiative and non-radiated recombination are increased, leading to the significant decrease of QW decay time. After the insertion of QD/PR, we might expect that the QW decay time is further reduced because of the FRET from the QWs into inserted QDs. However, the results show the QW decay time is slightly increased. Suh a result implies that the insertion of QD/PR can reduce the strain relaxation and/or the effect of surface defect states. Also, it implies that the FRET from the QWs into inserted QDs is indeed weak. The numbers inside the curly brackets show the FRET efficiencies in the sample series of QW-R-XXX. Generally speaking, with both GQD and RQD in a sample, the FRET efficiency is higher. The FRET efficiency cannot be evaluated in the sample series of QW-H-XXX because the QW (donor) condition has been changed in inserting QD/PR.

To further understand the causes for changing the emission behavior of the QWs, we use a QW template to fabricate a nano-hole array and then insert pure photoresist (without QD or Ag NP) into the nano-holes. Figure 4.16 shows the normalized QW PL spectra at 10 and 300 K for the intrinsic (I) case, and the other two cases of nano-hole (NH) fabrication and photoresist (PR) insertion. From the results in Fig. 4.16, we can evaluate the intrinsic IQE at 55.1 %, the IQE after nano-hole fabrication at 60.7 %, and that after photoresist insertion at 62.4 %. Figure 4.17 shows the PL decay profiles of the QW sample at the aforementioned three stages. We can see that the PL decay rate significantly increases after nano-hole fabrication. After pure photoresist insertion, the decay rate is reduced. The decay times are summarized in Table 4.2. Here, we can see that the decay time decreases from the

doi:10.6342/NTU202203112

intrinsic value of 20. 99 ns to 5.76 ns after nano-hole fabrication, and then increases to 8.06 ns after pure photoresist insertion. The opposite variation trends between IQE and PL decay time indicate that photoresist insertion can indeed reduce the effect of surface defect states on the nano-hole sidewall. In Table 4.1, we can see that the QW PL decay times after QD/PR insertion into the nano-holes of the sample series of QW-H-XXX are always shorter than 8.06 ns mentioned above. The differences of the QW PL decay time are caused by the FRET from the QWs into inserted QDs. Therefore, this FRET process does exists.

4.3 Continuous photoluminescence results

Figure 4.18 shows the normalized cw PL spectra of samples QW-X-GQD, QW-X-RQD, QW-X-GQD+GNP, and QW-X-RQD+RNP with X = R and H. All the spectra are normalized with respect to individual blue-light intensity peaks. Figure 4.19 shows the normalized cw PL spectra of samples QW-X-GQD+RQD, QW-X-GQD+RQD+GNP, and QW-X-GQD+RQD+RNP with X = R and H. All the spectra are normalized with respect to individual blue-light intensity peaks. For comparison, the result of sample QW-H-GQD+RQD before surface cleaning is also shown in Fig. 4.19. The integrated intensity ratios of G/B and R/B are shown inside the parentheses in Table 4.1.Here, we can see that generally the G/B or R/B ratios in the sample series of QW-H-XXX are smaller than the corresponding values in the sample series of QW-R-XXX because of the smaller QD quantities inside the nano-holes, when compared to those on the top surfaces. Also, the R/B ratios are generally higher than the G/B ratios due to the higher absorption of RQD at the QW emission wavelength. Meanwhile, the inclusion of Ag NPs generally results in a larger G/B and R/B ratios due to the enhanced FRTE from QW into QD and the increased QD emission efficiency. Furthermore, with both GQD and RQD in a sample, the FRET from GQD into RQD can lead to increased R/B ratios and decreased G/B ratios.

doi:10.6342/NTU202203112

4.4 Effects of reducing nano-hole depth

To confirm the speculation that the weak FRET from the QWs into inserted QDs is due to the significantly larger nano-hole depth, when compared to the thickness of the QW structure, we re-process the samples with the QW template. To reduce the nano-hole depth, we first remove the solidified photoresist solution of QD in the nano-holes and on the top surface of the sample series of QW-R-XXX and QW-H-XXX by combining the techniques of acetone immersion and O_2-plasma RIE. After this cleaning process, we fill into pure photoresist (no QD or Ag NP) into the nano-hole and clean the surface. Then, we use O_2-plasma RIE to etch the solidified pure photoresist in the nano-holes until the nano-hole depth reaches ~150 nm. Figures 4.20(a) and 4.20(b) show the atomic force microscopy (AFM) scanning image and a line-scan result, respectively, of a test sample, confirming that the new nano-hole depth is 151.79 nm. Next, we follow the procedures before to apply the photoresist solutions of QDs to various samples. Those new samples use the same designations as those before except that "(S)" is added at the end of a sample designation. Therefore, we now have a set of sample of a smaller nano-hole volume. The depth of ~152 nm can cover the whole QW structure on its sidewall (see Fig. 2.4). Figure 4.20(c) shows the schematic illustration of the structure of a re-processed sample demonstrating the use of pure photoresist to reduce the depth of a nano-hole from ~300 nm to ~152 nm for filling QD/PR.

Figures 4.21-4.31 show the PL decay profiles of the green, red, and blue lights in the re-processed samples, similar to those in Figs. 4.5-4.15, respectively. In Figs. 4.25-4.31 for the blue-light decay profiles, one more curve is added for each sample after the nano-holes are filled with pure photoresist up to the depth of ~152 nm. This curve is labeled by "after PR filling". The PL decay times of the re-processed samples are summarized in Table 4.3, similar to those in Table 4.1. However, in Table 4.3,

doi:10.6342/NTU202203112

one more value is added to the decay times of the QWs to describe the behavior after the nano-holes are filled with pure photoresist up to the depth of ~152 nm. Therefore, the four decay times separated by the three slashes correspond to the intrinsic case, the cases after nano-hole fabrication, after pure photoresist filling up to ~152 nm depth, and after QD/PR application and surface cleaning. One can see that in each sample, the QW PL decay time significantly decreases after nano-hole fabrication. Then, it increases slightly after pure photoresist filling. Next, it decreases again after QD/PR application and surface cleaning. The process of pure photoresist filling can reduce the effects of surface defect states and/or the strain relaxation, leading to an elongated PL decay time. Then, after QD insertion, the FRET from the QWs into QDs reduces the QW decay time. By comparing the results in Table 4.3 with those in Table 4.1, one can see that the corresponding decay times in the sample series of QW-R-XXX are comparable. However, the green and red-light (blue-light) decay times in the sample series of QW-H-XXX(S) are systematically longer (shorter) than the counterparts in the sample series of QW-H-XXX. This comparison result indicates that the effective FRET strength from the QWs into inserted QDs in the sample series of QW-H-XXX(S) is relatively higher. This is so because the quantity percentage of inserted QDs receiving FRET energy from the QWs is increased after the nano-holes are filled with pure photoresist up to the depth of ~152 nm. The numbers inside the curly brackets show the FRET efficiencies of those samples. Here, we can see that in the sample series of QW-R-XXX(S), the FRET efficiency in the sample of GQD or RQD only is around 20 %. After Ag NPs are added, that increases to a level of ~24 %. When both GQD and RQD exist in a sample, the FRET efficiency is further increased to ~30 %. After Ag NPs are added, that is further increased. RNP can more increase the FRET efficiency from the QWs into QDs, when compared with GNP. The variation trend of FRET efficiency in the sample series of QW-H-XXX(S) is the same as that in the sample series of QW-R-XXX(S). However, the corresponding values are relatively higher

doi:10.6342/NTU202203112

by 3-6 %.

Figures 4.32 and 4.33 show the normalized PL spectra of the re-processed samples, similar to those in Figs. 4.18 and 4.19, respectively. The integrated intensity ratios G/B and R/B are also shown in Table 4.3 inside the parentheses. Here, one can see that in the sample series of QW-R-XXX(S), the G/B ratios are increased. When both GQD and RQD exist in a sample, the stronger green intensity also leads to a stronger red intensity (through FRET) and hence a larger R/B ratio. In the sample series of QW-H-XXX(S), both G/B and R/B ratios are generally increased indicating the effectively stronger FRET from the QWs into QDs.

doi:10.6342/NTU202203112

Table 4.1 PL decay times of the samples based on the QW template under different conditions. For samples QW-R-XXX, the two PL decay times correspond to the cases before and after nano-hole fabrication. For samples QW-H-XXX, the three PL decay times correspond to the cases before and after nano-hole fabrication, and after QD/Ag NP application (after surface cleaning). The numbers inside the parentheses show the G/B and R/B ratios. The underlined numbers show the results of sample QW-H-GQD+RQD before surface cleaning. The numbers inside the curly brackets show the FRET efficiencies.

XXX =		QW-R-XXX (ns)	QW-H-XXX (ns)
GQD	B	18.08/14.14 (1) {21.79 %}	18.14/5.44/6.06 (1)
	G	6.43 (1.38)	5.84 (0.13)
RQD	B	18.11/15.36 (1) {15.18 %}	19.19/4.43/5.63 (1)
	R	9.52 (3.95)	7.29 (1.64)
GQD+GNP	B	16.80/11.24 (1) {33.10 %}	18.71/5.25/6.43 (1)
	G	5.65 (2.19)	4.95 (0.19)
RQD+RNP	B	18.05/14.33 (1) {20.61 %}	20.06/4.28/5.75 (1)
	R	9.06 (5.83)	6.54 (3.21)
GQD+RQD	B	19.92/13.88 (1) {30.32 %}	20.61/5.84/6.33/<u>6.32</u> (1)
	G	4.96 (1.55)	3.59/<u>4.86</u> (0.08/<u>1.63</u>)
	R	11.81 (7.98)	7.99/<u>11.01</u> (0.52/<u>8.49</u>)
GQD+RQD+GNP	B	16.62/10.68 (1) {35.74 %}	19.50/3.41/4.58 (1)
	G	4.64 (2.05)	3.29 (0.17)
	R	11.28 (9.92)	7.85 (0.94)
GQD+RQD+RNP	B	18.36/12.16 (1) {33.77 %}	20.37/4.98/4.70 (1)
	G	4.32 (1.20)	3.18 (0.11)

doi:10.6342/NTU202203112

	R	10.62 (6.96)	7.53 (0.85)

doi:10.6342/NTU202203112

Table 4.2 IQE and PL decay times of a test QW sample after different process stages.

	Intrinsic	After nano-hole fabrication	After pure photoresist insertion
IQE (%)	55.1	60.7	62.4
PL decay time (ns)	20.99	5.76	8.06

doi:10.6342/NTU202203112

Table 4.3 PL decay times of samples QW-R-XXX(S) and QW-H-XXX(S) under different conditions, similar to the results in Table 4.1.

XXX =		QW-R-XXX(S) (ns)	QW-H-XXX(S) (ns)
GQD	B	18.17/14.46 (1) {20.42 %}	18.14/4.71/6.31/4.70 (1) {25.52 %}
	G	6.47 (2.99)	5.98 (0.26)
RQD	B	18.21/14.51 (1) {20.32 %}	19.19/4.01/6.01/4.53 (1) {24.63 %}
	R	9.28 (3.98)	9.07 (1.44)
GQD+GNP	B	17.60/13.37 (1) {24.03 %}	18.71/5.15/6.43/4.49 (1) {30.17 %}
	G	5.74 (3.72)	5.23 (0.48)
RQD+RNP	B	18.28/13.77 (1) {24.67 %}	20.06/4.39/5.91/4.19 (1) {29.10 %]
	R	8.89 (5.65)	8.68 (2.34)
GQD+RQD	B	18.81/13.01 {30.84 %}	20.61/4.78/6.52/4.35 {33.28 %}
	G	5.61 (2.85)	5.04 (0.20)
	R	11.48 (13.52)	10.83 (1.21)
GQD+RQD +GNP	B	17.49/11.74 {32.88 %}	19.50/3.86/5.82/3.68 {36.77 %}
	G	4.91 (3.54)	4.62 (0.31)
	R	10.85 (15.61)	10.42 (1.56)
GQD+RQD +RNP	B	18.56/12.16 {34.48 %}	20.37/4.69/6.96/4.23 {39.22 %}
	G	4.85 (3.38)	4.32 (0.28)
	R	10.53 (17.80)	9.43 (1.91)

doi:10.6342/NTU202203112

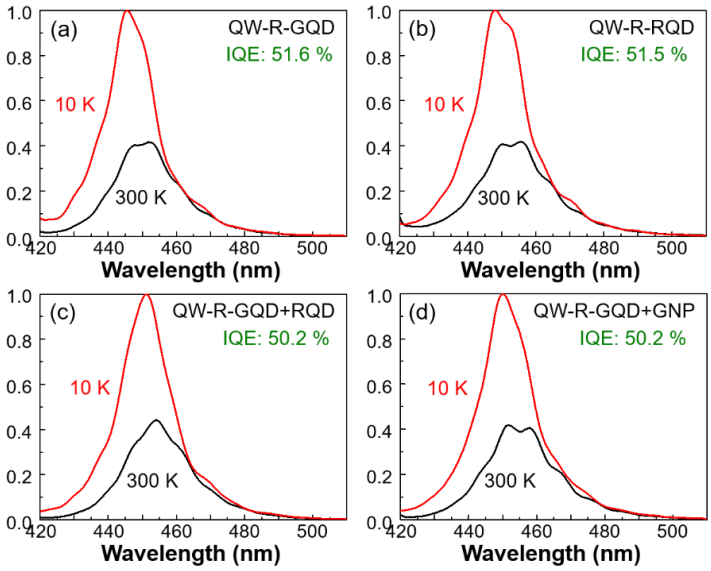

Fig. 4.1 (a)-(d): Normalized PL spectra at 10 and 300 K for evaluating IQEs in samples QW-R-GQD, QW-R-RQD, QW-R-GQD+RQD, and QW-R-GQD+GNP, respectively. The IQE values are also shown in the figures.

doi:10.6342/NTU202203112

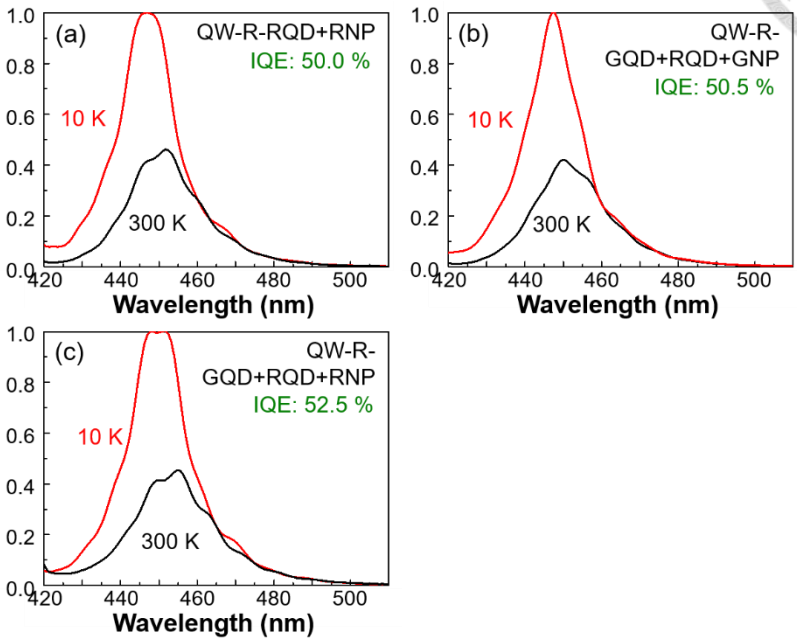

Fig. 4.2 (a)-(c): Normalized PL spectra at 10 and 300 K for evaluating IQEs in samples QW-R-RQD+RNP, QW-R-GQD+RQD+GNP, and QW-R-GQD+RQD+RNP, respectively. The IQE values are also shown in the figures.

doi:10.6342/NTU202203112

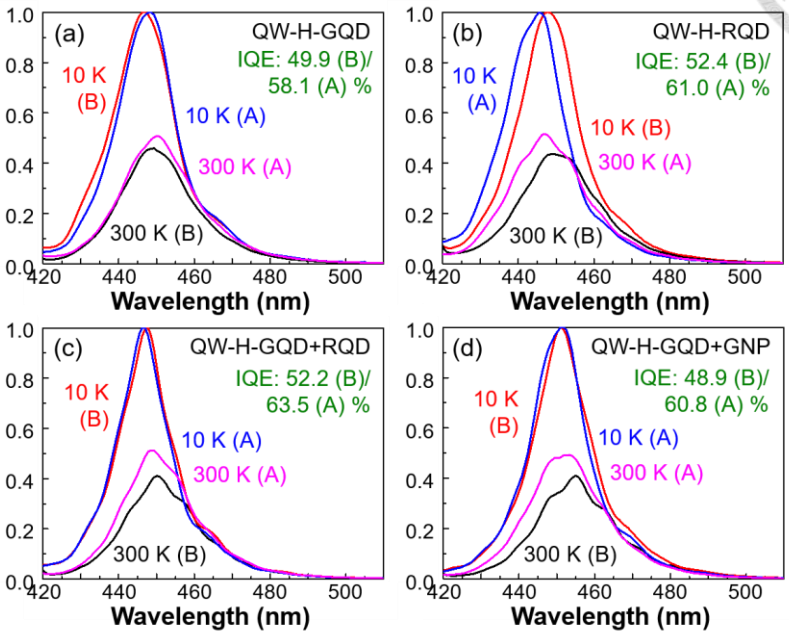

Fig. 4.3 (a)-(d): Normalized PL spectra at 10 and 300 K for evaluating IQEs in samples QW-H-GQD, QW-H-RQD, QW-H-GQD+RQD, and QW-H-GQD+GNP, respectively, before (B) and after (A) nano-hole fabrication. The IQE values are also shown in the figures.

doi:10.6342/NTU202203112

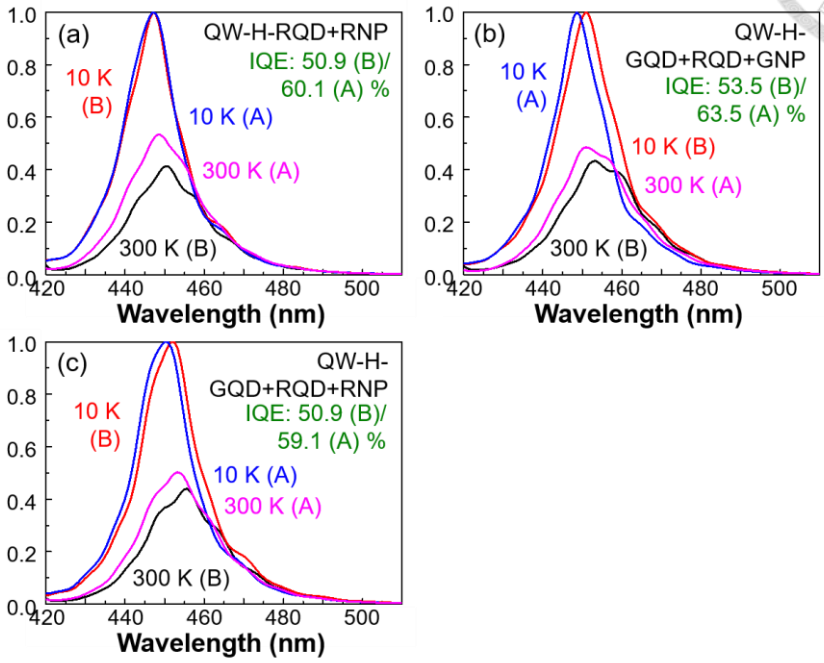

Fig. 4.4 (a)-(c): Normalized PL spectra at 10 and 300 K for evaluating IQEs in samples QW-H-RQD+RNP, QW-H-GQD+RQD+GNP, and QW-H-GQD+RQD+RNP, respectively, before (B) and after (A) nano-hole fabrication. The IQE values are also shown in the figures.

doi:10.6342/NTU202203112

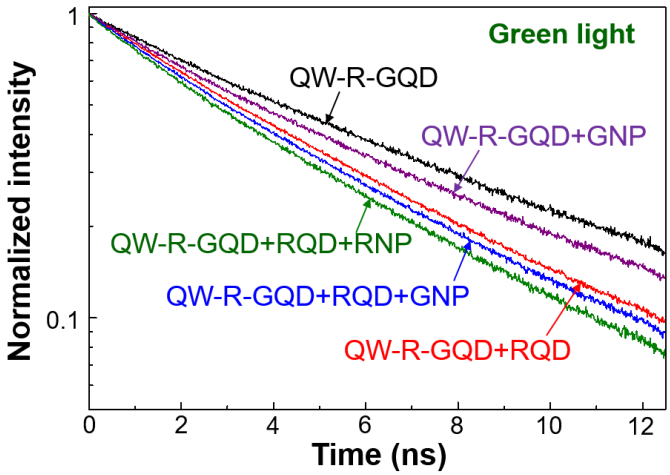

Fig. 4.5 Normalized green-light PL decay profiles of samples QW-R-GQD, QW-R-GQD+GNP, QW-R-GQD+RQD, QW-R-GQD+RQD+GNP, and QW-R-GQD+RQD+RNP.

doi:10.6342/NTU202203112

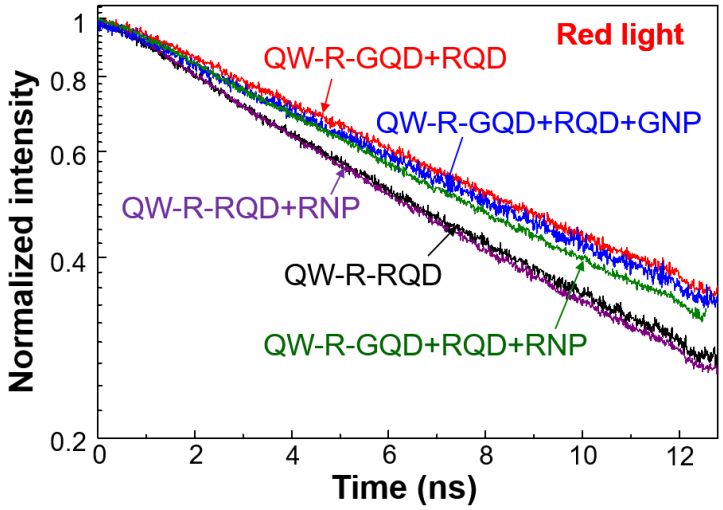

Fig. 4.6 Normalized red-light PL decay profiles of samples QW-R-RQD, QW-R-RQD+RNP, QW-R-GQD+RQD, QW-R-GQD+RQD+GNP, and QW-R-GQD+RQD+RNP.

doi:10.6342/NTU202203112

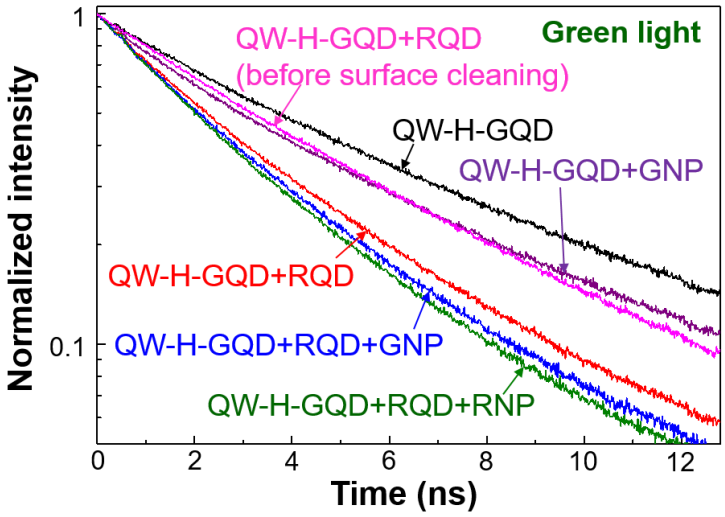

Fig. 4.7 Normalized green-light PL decay profiles of samples QW-H-GQD, QW-H-GQD+GNP, QW-H-GQD+RQD, QW-H-GQD+RQD+GNP, and QW-H-GQD+RQD+RNP. For comparison, that of sample QW-H-GQD+RQD before surface cleaning is also shown.

doi:10.6342/NTU202203112

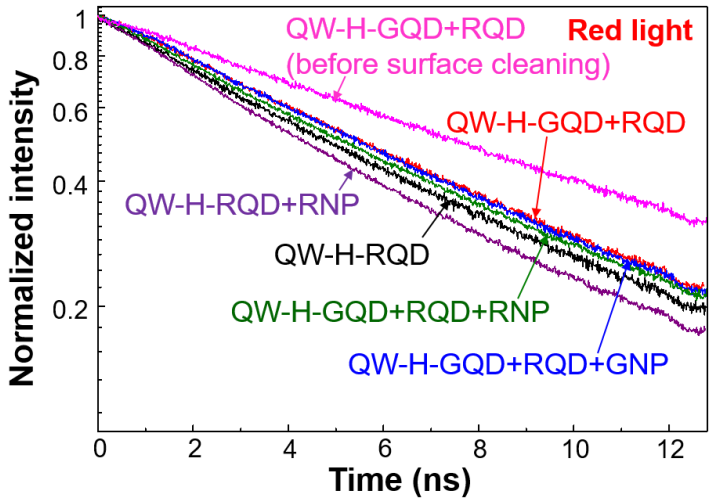

Fig. 4.8 Normalized red-light PL decay profiles of samples QW-H-RQD, QW-H-RQD+RNP, QW-H-GQD+RQD, QW-H-GQD+RQD+GNP, and QW-H-GQD+RQD+RNP. For comparison, that of sample QW-H-GQD+RQD before surface cleaning is also shown.

doi:10.6342/NTU202203112

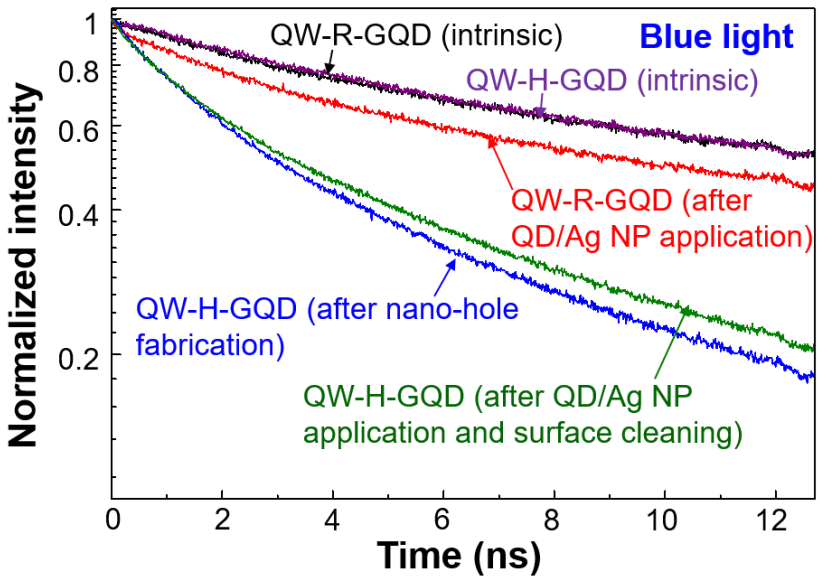

Fig. 4.9 Normalized blue-light PL decay profiles of samples QW-R-GQD and QW-H-GQD under different conditions. For sample QW-R-GQD, the results include the intrinsic condition and that after QD/Ag NP application. For sample QW-H-GQD, the results include the intrinsic condition, that after nano-hole application, and that after QD/Ag NP application and surface cleaning.

doi:10.6342/NTU202203112

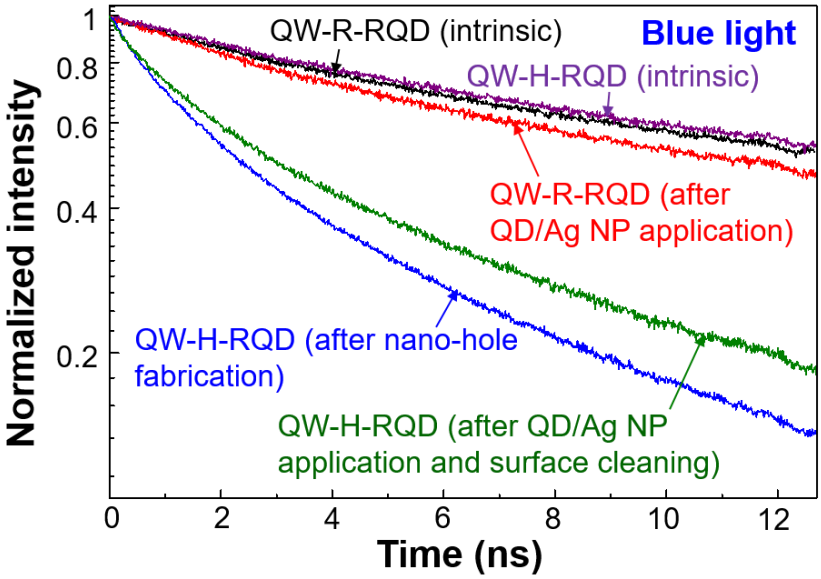

Fig. 4.10 Normalized blue-light PL decay profiles of samples QW-R-RQD and QW-H-RQD under different conditions, similar to Fig. 9.

doi:10.6342/NTU202203112

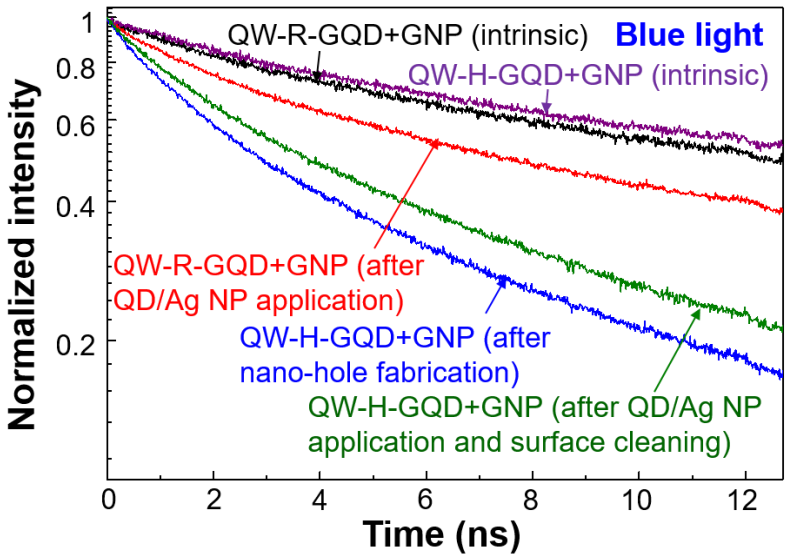

Fig. 4.11 Normalized blue-light PL decay profiles of samples QW-R-GQD+GNP and QW-H-GQD+GNP under different conditions, similar to Fig. 9.

doi:10.6342/NTU202203112

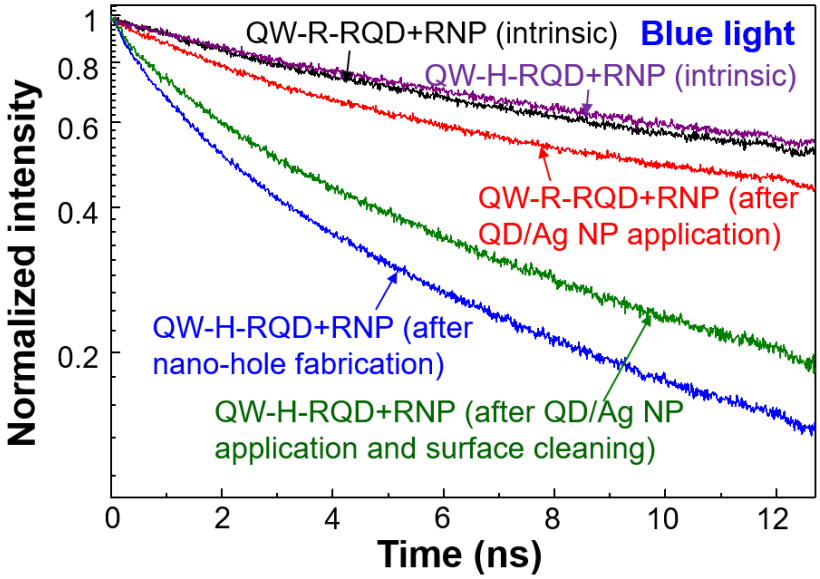

Fig. 4.12 Normalized blue-light PL decay profiles of samples QW-R-RQD+RNP and QW-H-RQD+RNP under different conditions, similar to Fig. 9.

doi:10.6342/NTU202203112

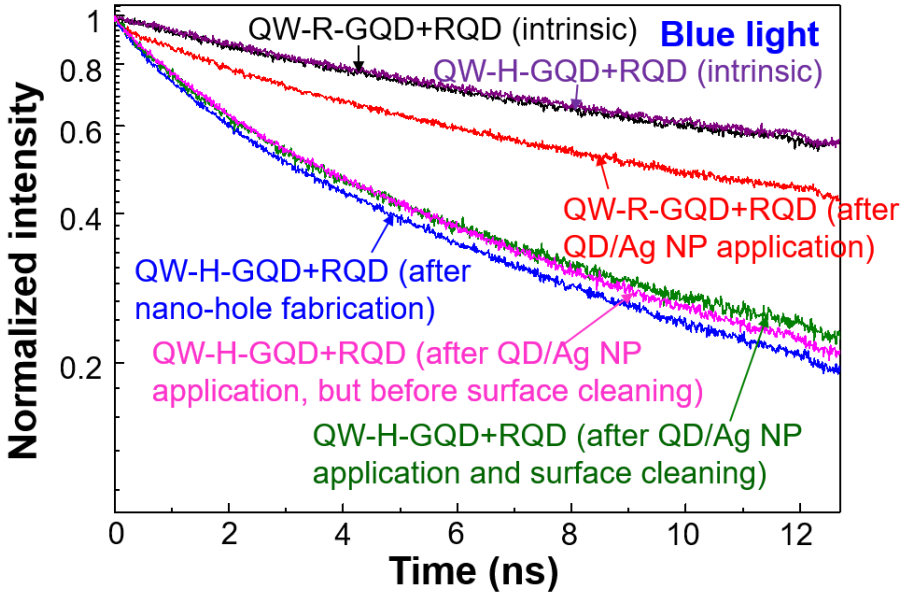

Fig. 4.13 Normalized blue-light PL decay profiles of samples QW-R-GQD+RQD and QW-H-GQD+RQD under different conditions, similar to Fig. 9. For comparison, that of sample QW-H-GQD+RQD before surface cleaning is also shown.

doi:10.6342/NTU202203112

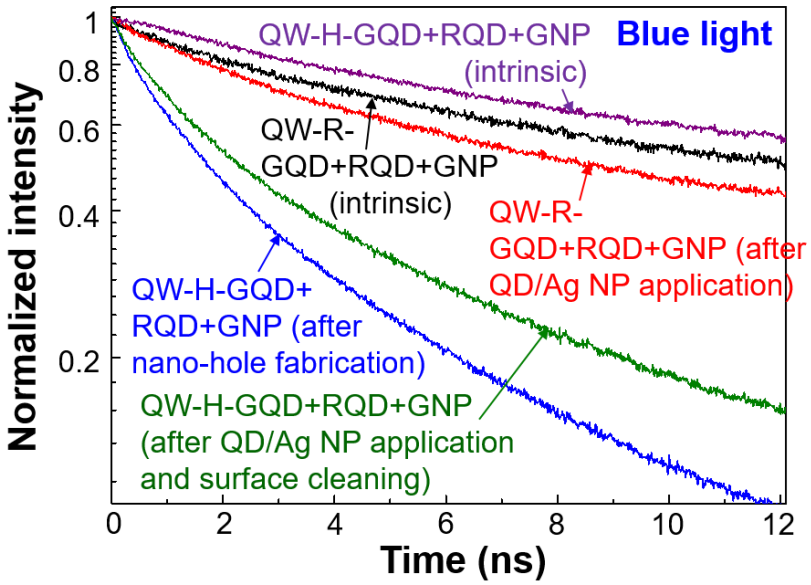

Fig. 4.14 Normalized blue-light PL decay profiles of samples QW-R-GQD+RQD+GNP and QW-H-GQD+RQD+GNP under different conditions, similar to Fig. 9.

doi:10.6342/NTU202203112

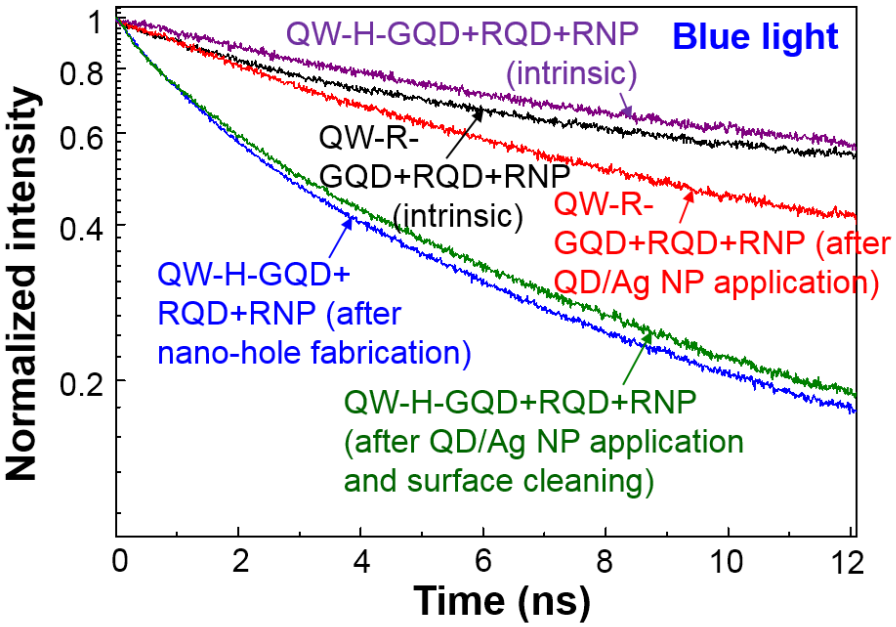

Fig. 4.15 Normalized blue-light PL decay profiles of samples QW-R-GQD+RQD+RNP and QW-H-GQD+RQD+RNP under different conditions, similar to Fig. 9.

doi:10.6342/NTU202203112

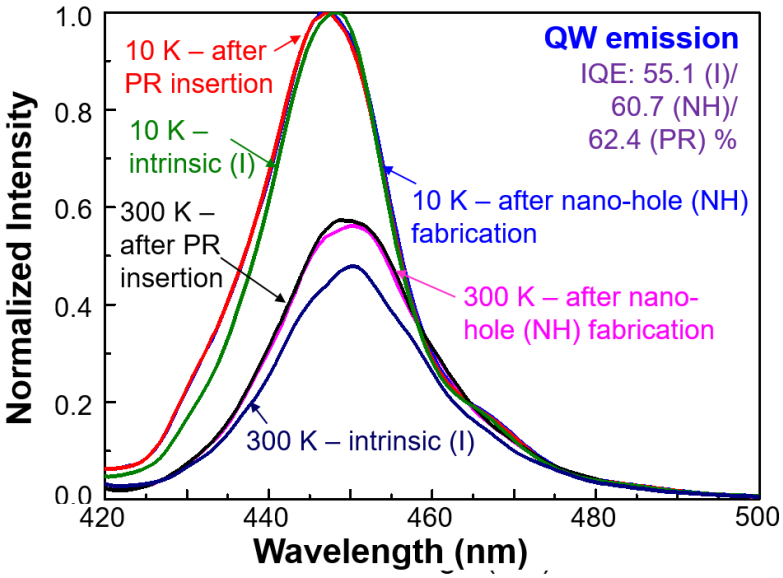

Fig. 4.16 Normalized PL spectra at 10 and 300 of a test sample after nano-hole fabrication and PR filling.

doi:10.6342/NTU202203112

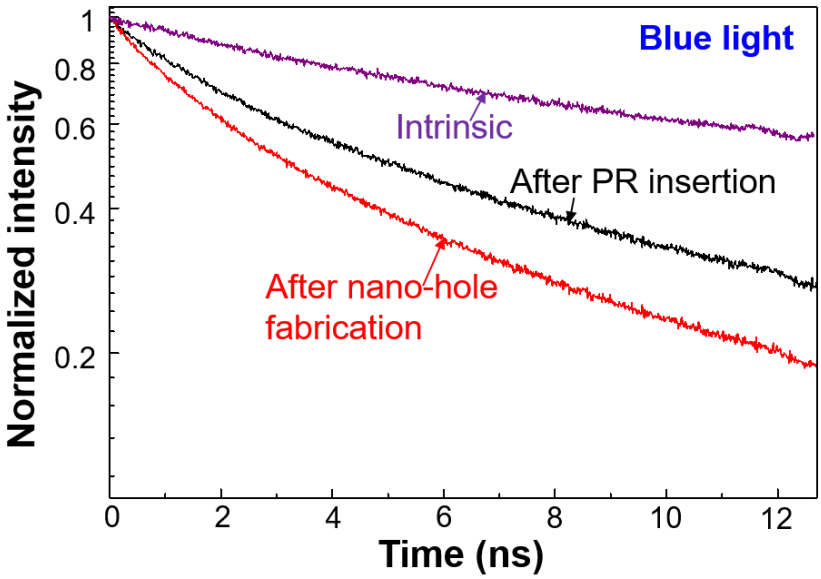

Fig. 4.17 Normalized PL decay profiles of the test sample after nano-hole fabrication and PR filling.

doi:10.6342/NTU202203112

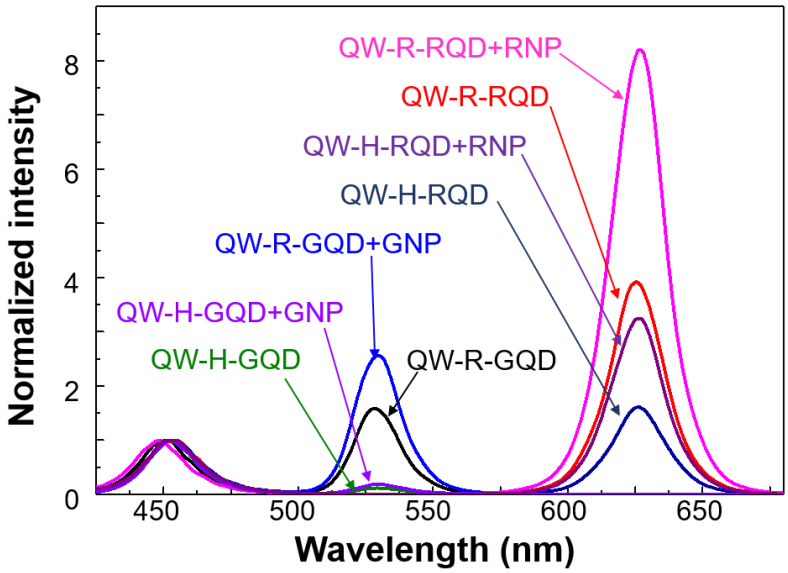

Fig. 4.18 Normalized PL spectra of samples QW-R-GQD, QW-R-RQD, QW-R-GQD+GNP, QW-R-RQD+RNP, QW-H-GQD, QW-H-RQD, QW-H-GQD+GNP, and QW-H-RQD+RNP. All the spectra are normalized with respect to individual blue-light peak intensities.

doi:10.6342/NTU202203112

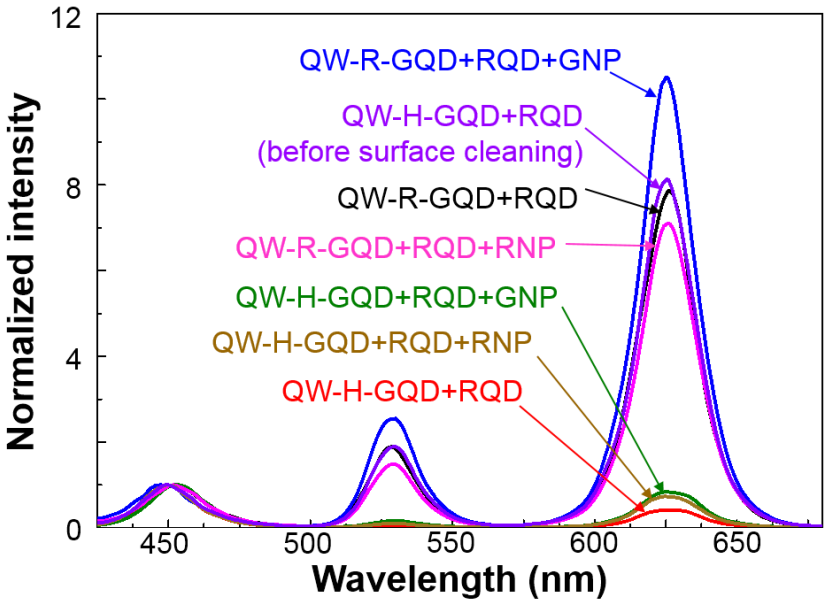

Fig. 4.19 Normalized PL spectra of samples QW-R-GQD+RQD, QW-R-GQD+RQD+GNP, QW-R-GQD+RQD+RNP, QW-H-GQD+RQD, QW-H-GQD+RQD+GNP, and QW-H-GQD+RQD+RNP. All the spectra are normalized with respect to individual blue-light peak intensities. For comparison, that of sample QW-H-GQD+RQD before surface cleaning is also shown.

doi:10.6342/NTU202203112

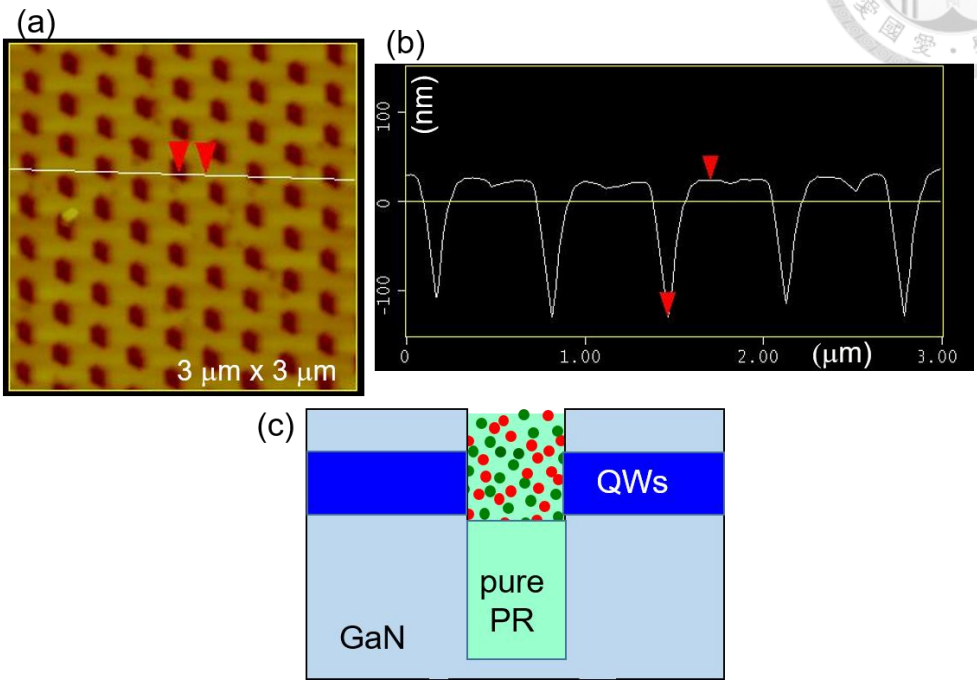

Fig. 4.20 (a): AFM image of the nano-holes in a re-processed sample. (b): Line-scan result showing the nano-hole depth at ~152 nm. (c): Schematic illustration of the structure of a re-processed sample showing the use of pure photoresist to reduce the depth of a nano-hole from ~300 nm to ~152 nm for filling QD/PR.

doi:10.6342/NTU202203112

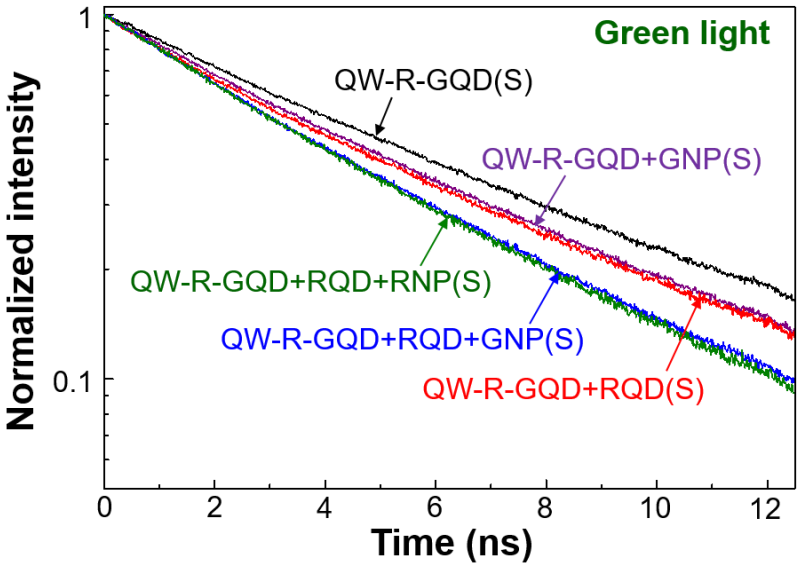

Fig. 4.21 Normalized PL decay profiles for the sample series of QW-R-XXX(S) and/or QW-H-XXX(S), similar to those in Fig. 4.5.

doi:10.6342/NTU202203112

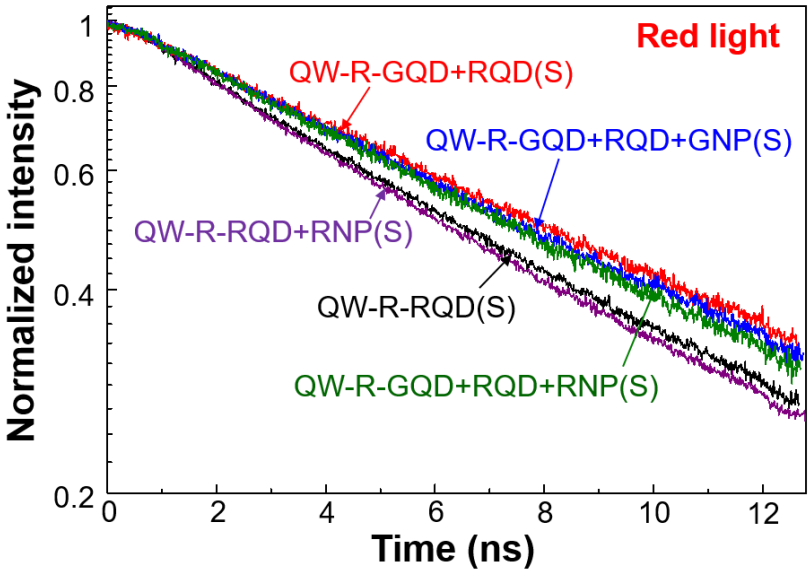

Fig. 4.22 Normalized PL decay profiles for the sample series of QW-R-XXX(S) and/or QW-H-XXX(S), similar to those in Fig. 4.6.

doi:10.6342/NTU202203112

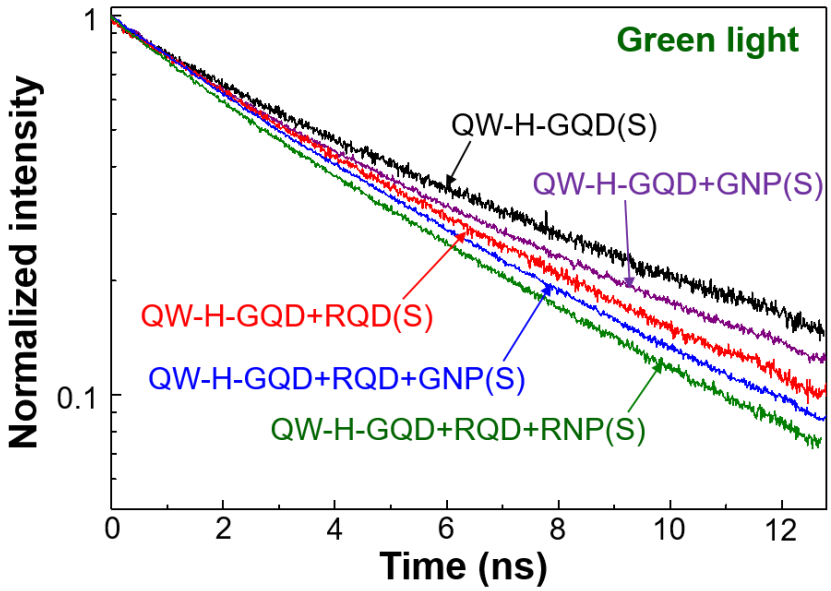

Fig. 4.23 Normalized PL decay profiles for the sample series of QW-R-XXX(S) and/or QW-H-XXX(S), similar to those in Fig. 4.7.

doi:10.6342/NTU202203112

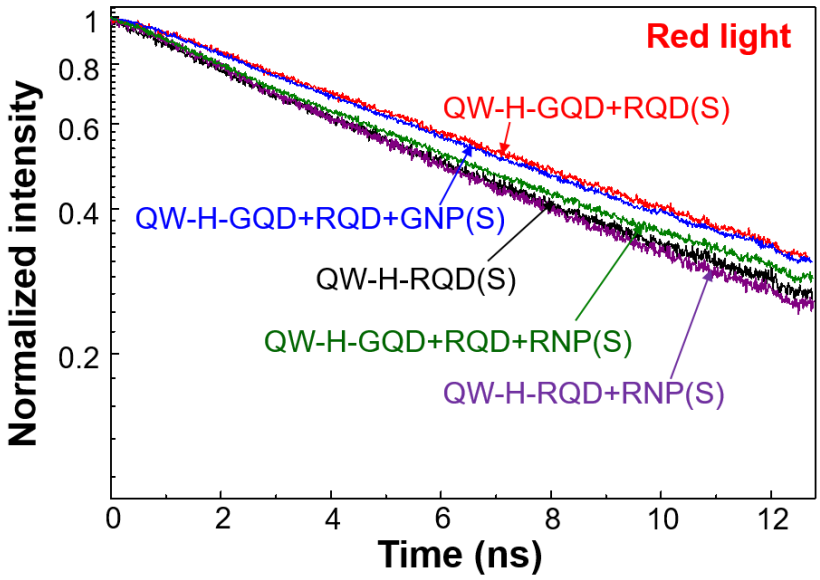

Fig. 4.24 Normalized PL decay profiles for the sample series of QW-R-XXX(S) and/or QW-H-XXX(S), similar to those in Fig. 4.8.

doi:10.6342/NTU202203112

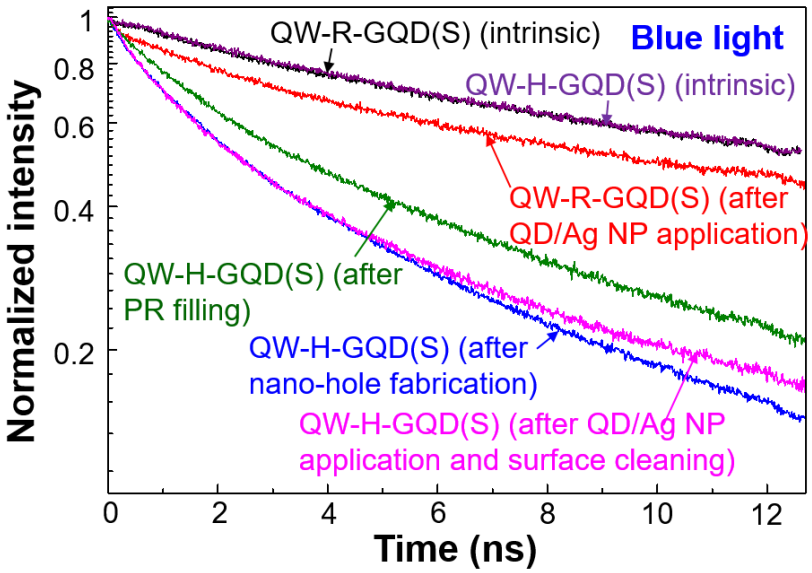

Fig. 4.25 Normalized PL decay profiles for the sample series of QW-R-XXX(S) and/or QW-H-XXX(S), similar to those in Fig. 4.9.

doi:10.6342/NTU202203112

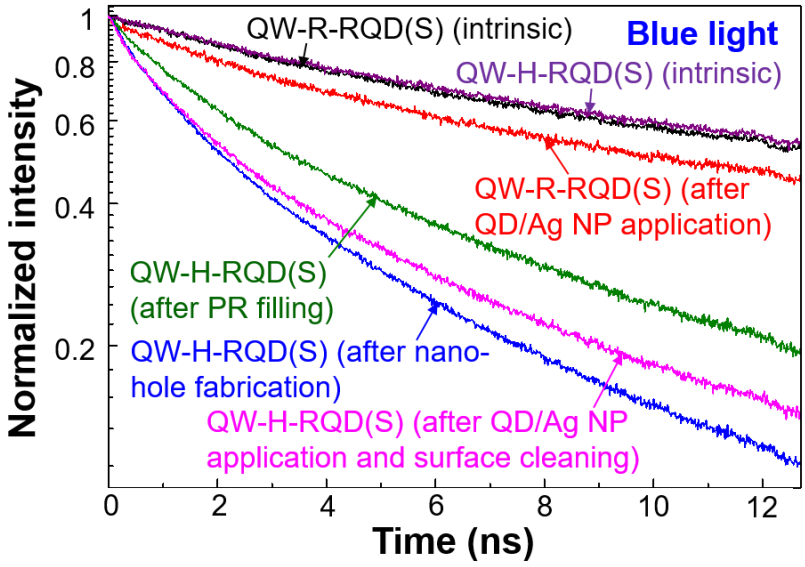

Fig. 4.26 Normalized PL decay profiles for the sample series of QW-R-XXX(S) and/or QW-H-XXX(S), similar to those in Fig. 4.10.

doi:10.6342/NTU202203112

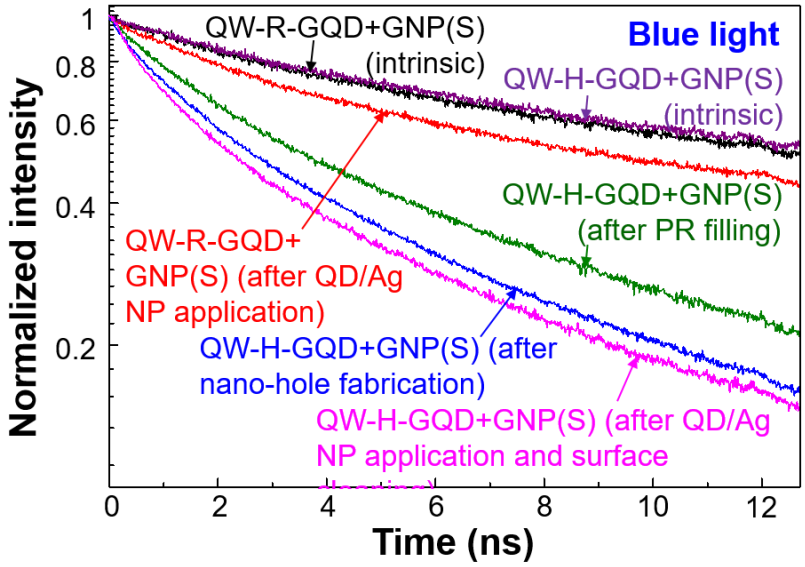

Fig. 4.27 Normalized PL decay profiles for the sample series of QW-R-XXX(S) and/or QW-H-XXX(S), similar to those in Fig. 4.11.

doi:10.6342/NTU202203112

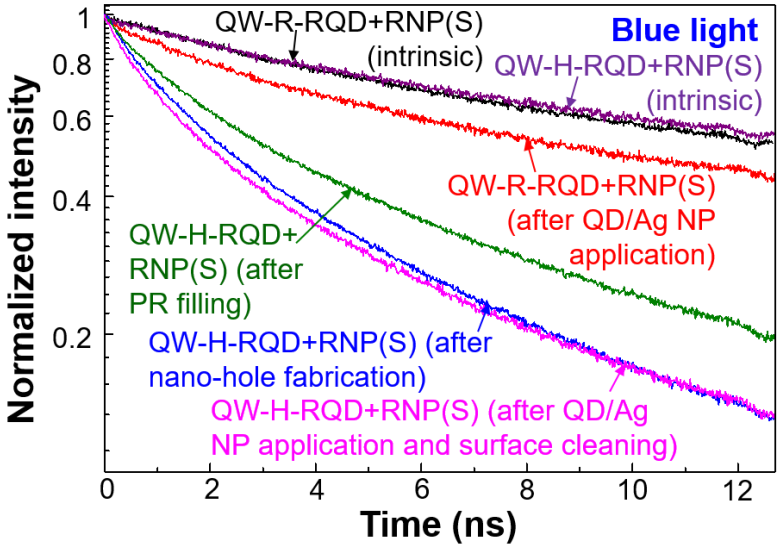

Fig. 4.28 Normalized PL decay profiles for the sample series of QW-R-XXX(S) and/or QW-H-XXX(S), similar to those in Fig. 4.12.

doi:10.6342/NTU202203112

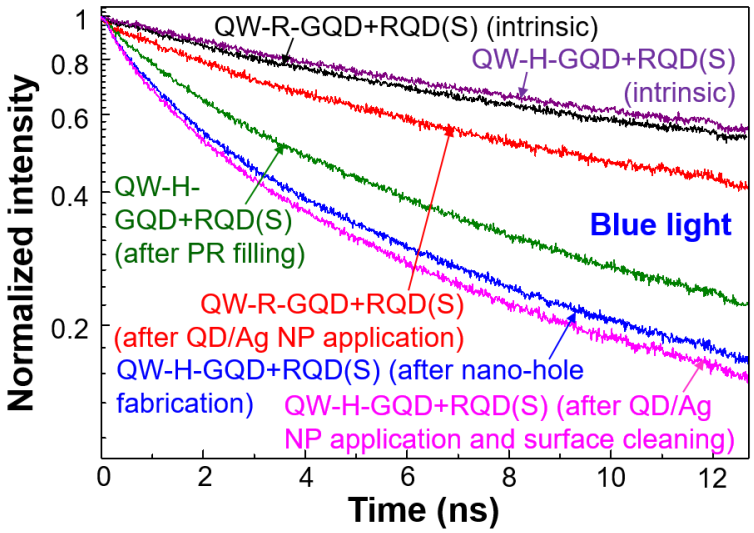

Fig. 4.29 Normalized PL decay profiles for the sample series of QW-R-XXX(S) and/or QW-H-XXX(S), similar to those in Fig. 4.13.

doi:10.6342/NTU202203112

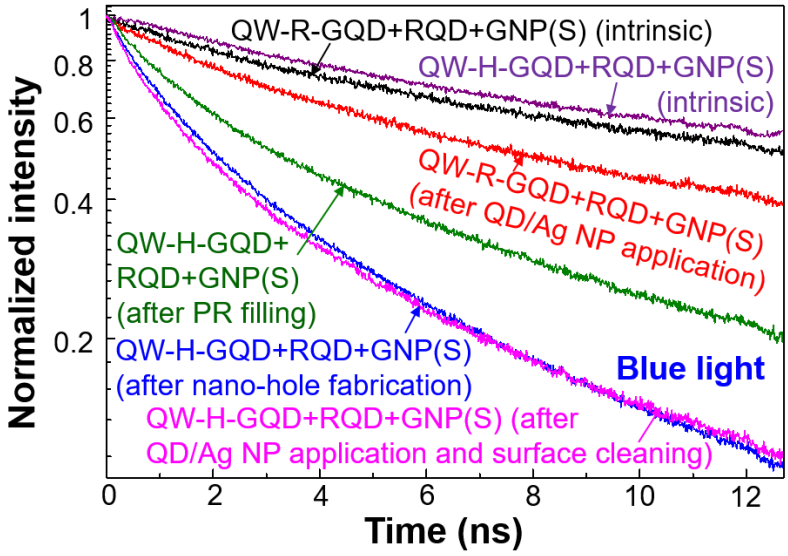

Fig. 4.30 Normalized PL decay profiles for the sample series of QW-R-XXX(S) and/or QW-H-XXX(S), similar to those in Fig. 4.14.

doi:10.6342/NTU202203112

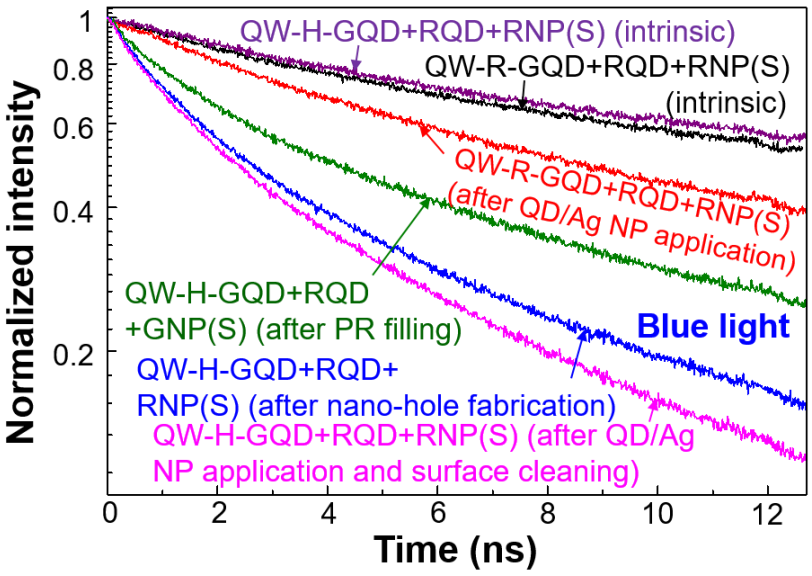

Fig. 4.31 Normalized PL decay profiles for the sample series of QW-R-XXX(S) and/or QW-H-XXX(S), similar to those in Fig. 4.15.

doi:10.6342/NTU202203112

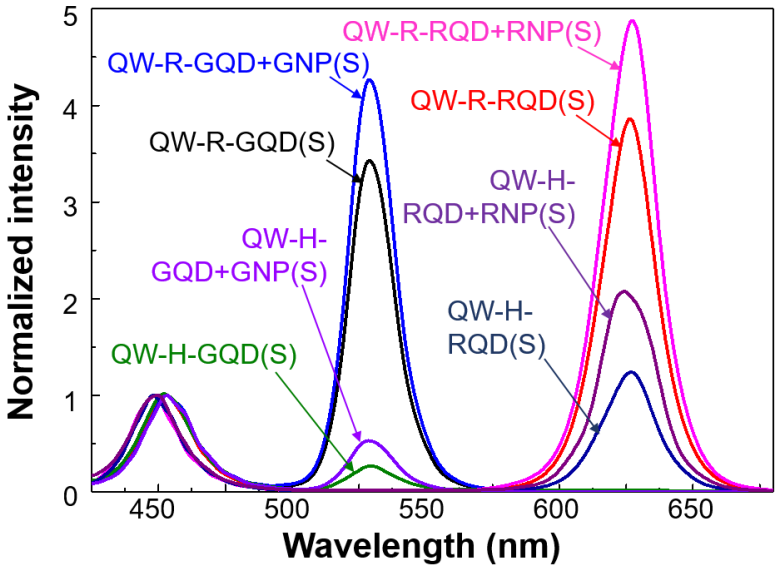

Fig. 4.32 Normalized PL spectra for the sample series of QW-R-XXX(S) and/or QW-H-XXX(S), similar to those in Fig. 4.18.

doi:10.6342/NTU202203112

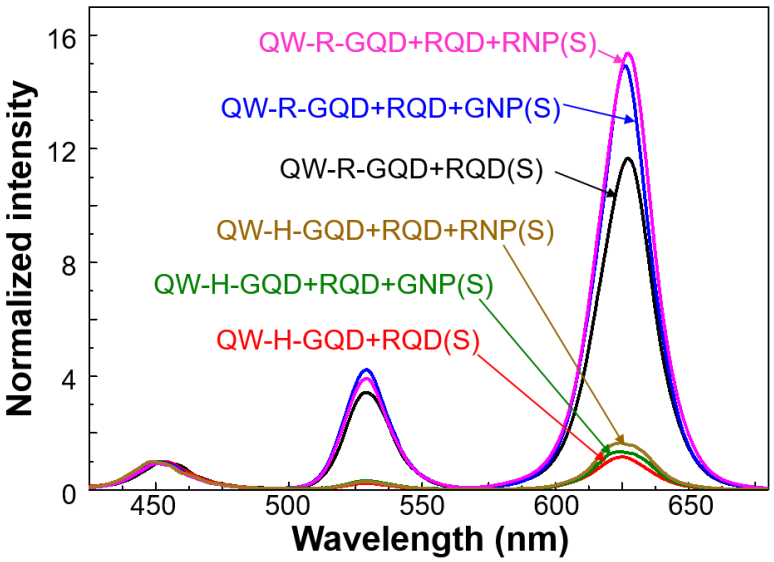

Fig. 4.33 Normalized PL spectra for the sample series of QW-R-XXX(S) and/or QW-H-XXX(S), similar to those in Fig. 4.19.

doi:10.6342/NTU202203112

Chapter 5 Color Conversion of Colloidal Quantum Dot Affected by the Surface Plasmon Coupling between Surface Ag Nanoparticles and a Quantum-well Structure

5.1 General descriptions of the samples

Figures 5.1(a) and 5.1(b) illustrate the sample structures to be fabricated for studying the SP coupling effect induced by the surface Ag NPs on the FRET from the QWs into the QDs inserted in a shallow nano-hole. Figures 5.2(a) and 5.2(b) show the plane-view SEM images of different magnifications of a shallow nano-hole sample. Here, we can see that with shallow etching, the top morphology of the hole is not as uniform as that with deep etching, as shown in Fig. 2.6(b). Figures 5.3(a) and 5.3(b) show the cross-sectional SEM images of different magnifications of the shallow nano-hole sample. Here, one can see that the hole depth is ~40 nm. Referred to Fig. 2.4, we can see that the bottom of such a shallow is ~10 nm above the top QW in the QW template. We then follow the aforementioned procedure for inserting the photoresist solution of QDs into the shallow nano-holes and cleaning the surface. Three QD samples are prepared, including those with pure GQD (sample QW-HP-GQD), pure RQD (sample QW-HP-RQD), and GQD plus RQD (sample QW-HP-GQD+RQD). After the top surfaces of the three samples are cleaned, we deposit 2.5-nm Ag onto the surfaces of the samples at room temperature. With thermal annealing, surface Ag NPs can be naturally formed as shown in the SEM images of Figs. 5.4(a) and 5.4(b). The surface Ag NPs on the three samples lead to the transmission spectra shown in Fig. 5.5. The depression minima of the three curves are all around 530 nm. The three vertical dashed lines indicate the emission wavelengths of the QW (445 nm), GQD (530 nm), and RQD (625 nm), showing that the broad LSP resonance feature of the deposited surface Ag NPs can cover all the three emission wavelengths. However, it is noted that the

doi:10.6342/NTU202203112

broad LPS resonance feature is caused by the distribution of surface Ag NPs on photoresist (refractive index at 1.577) and GaN (refractive index at 2.399). The former (latter) results in the LSP feature on the shorter- (longer-) wavelength side. In this study, only those surface Ag NPs on the QD/PR filled nano-holes can effectively influence the FRET from the QWs into QDs. Although we cannot differentiate the LSP resonance contributions from the two parts of surface Ag NPs, the emissions of the QWs, GQDs, and RQDs must be all affected by the SP coupling. In particular, those of the QWs and GQDs must be significantly influenced by the SP coupling process.

Figure 5.6(a) shows the normalized PL spectra at 10 and 300 K of sample QW-HP-GQD before (B) and after (A) nano-hole fabrication. From the integrated intensity ratios, we can obtain the IQEs before and after nano-hole fabrication at 58.5 and 60.4 %, respectively. Figures 5.6(a) and 5.6(b) show the results of samples QW-HP-RQD and QW-HP-GQD+RQD, respectively, similar to those in Fig. 5.6(a) for sample QW-HP-GQD. After nano-hole fabrication, the IQE of the QWs is slightly increased. However, the increments are significantly smaller than those after fabricating deep nano-holes (300 nm in depth), as shown in Figs. 4.3 and 4.4. This is so because strain relaxation is weaker after shallow nano-hole fabrication. .

5.2 Results of time-resolved and continuous photoluminescence measurements

Figure 5.7 shows the green-light PL decay profiles of samples QW-HP-GQD and QW-HP-GQD+RQD before (w/o SP) and after (SP) surface Ag NP deposition. Here, one can see that with SP coupling, the PL decay rate is slightly decreased. Figure 5.8 shows the red-light PL decay profiles of samples QW-HP-RQD and QW-HP-GQD+RQD before (w/o SP) and after (SP) surface Ag NP deposition. Here, we can see that the difference of red-light decay rate between the cases with and without SP coupling becomes larger. Figures 5.9-5.11 show the blue-light PL decay profiles of

doi:10.6342/NTU202203112

samples QW-HP-GQD, QW-HP-RQD and QW-HP-GQD+RQD, respectively, in the intrinsic case and the cases after nano-hole fabrication, after QD/PR application, and after surface Ag NP deposition. All the samples show that the blue-light PL decay rate increases after nano-hole fabrication, further increases after QD/PR application, and further increases after surface Ag NP deposition. After nano-hole fabrication, strain relaxation and defect increase can lead to a higher decay rate. After QD/PR application, the FRET from the QWs into QDs leads to a further increase of blue-light decay rate. Finally, after Ag NP deposition, the induced SP coupling results in the enhanced FRET from the QWs into QDs.

Table 5.1 summarizes the PL decay times of the three samples under different conditions. We can see that the increments of green-light decay time in sample QW-HP-GQD and red-light decay time in sample QW-HP-RQD after surface Ag NP deposition are small, indicating that the SP coupling effect on the FRET from the QWs into QDs is not very strong. In sample QW-HP-GQD+RQD, although the increment of green-light decay time is small, that of red light is quite large. This result is caused by the FRET from GQD into RQD. The numbers inside the curly brackets show the efficiencies of FRET from the QWs into QDs before Ag NP deposition. Those FRET efficiencies are not high.

Figure 5.12 shows the normalized PL spectra of those three samples before and after Ag NP deposition. All the spectra are normalized with respect to the individual blue peak intensities. The numbers inside the parentheses in Table 5.1 show the integrated intensity ratios G/B and R/B in those three samples. Here, we can see that the SP coupling can increase the G/B and R/B ratios. In other words, the SP coupling through the surface Ag NPs can enhance the FRET from the QWs into the QDs inserted into the shallow nano-holes.

doi:10.6342/NTU202203112

Table 5.1 PL decay times of blue-, green, and red-light in samples QW-HP-GQD, QW-HP-RQD, and QW-HP-GQD+RQD under different conditions. The numbers inside the parentheses show the integrated intensity ratios G/B and R/B. The numbers inside the curly brackets show the FRET efficiencies before Ag NP deposition.

Sample		Intrinsic (ns)	After nano-hole fabrication (ns)	After QD/PR application (ns)	After Ag NP deposition (ns)
QW-HP-GQD	B	10.61	7.13	6.46 {9.40 %}	5.81
	G	---	---	7.08 (0.15)	7.23 (0.24)
QW-HP-RQD	B	10.11	7.26	6.13 {15.57 %}	5.72
	R	---	---	10.11 (0.41)	10.87 (0.77)
QW-HP-GQD+RQD	B	9.91	7.22	6.01 {16.76 %}	5.45
	G	---	---	6.66 (0.12)	6.77 (0.16)
	R	---	---	11.75 (0.52)	13.07 (0.72)

doi:10.6342/NTU202203112

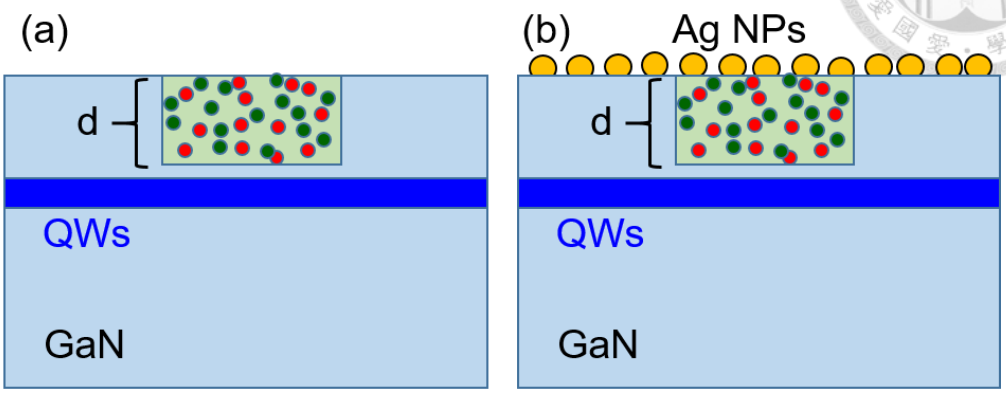

Fig. 5.1 (a) and (b): Schematic illustrations of the structures of samples QW-HP-GQD, QW-HP-RQD, and QW-HP-GQD+RQD before and after surface Ag NP deposition.

doi:10.6342/NTU202203112

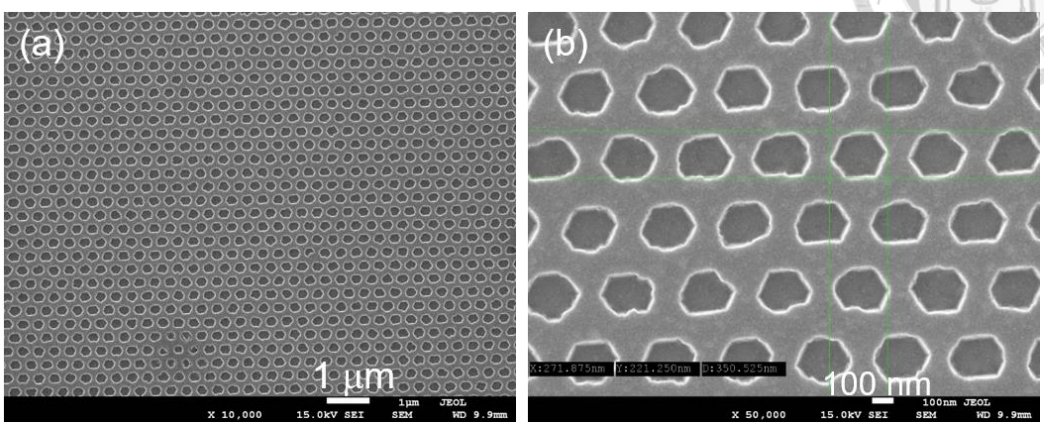

Fig. 5.2 (a) and (b): Plane-view SEM images with different magnifications of a test sample with surface shallow nano-holes.

doi:10.6342/NTU202203112

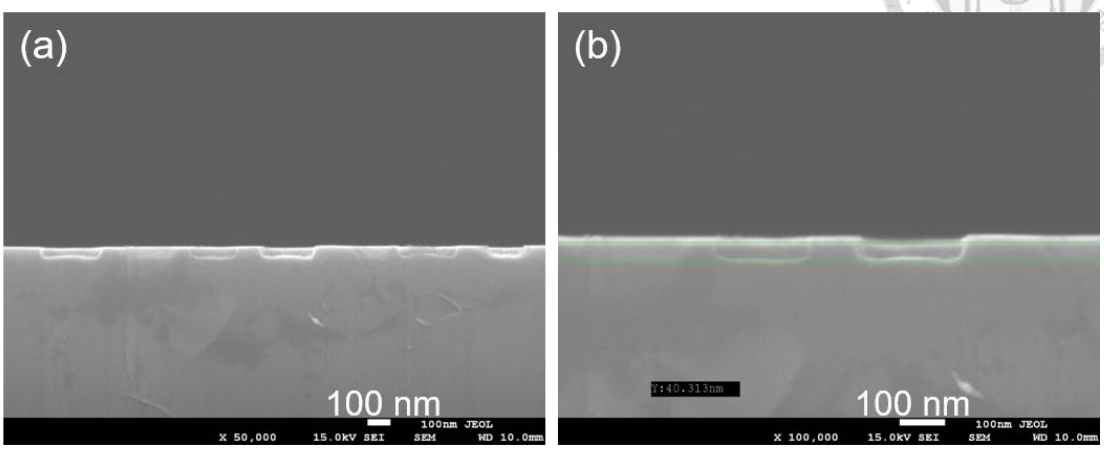

Fig. 5.3 (a) and (b): Cross-sectional SEM images with different magnifications of a test sample with surface shallow nano-holes.

doi:10.6342/NTU202203112

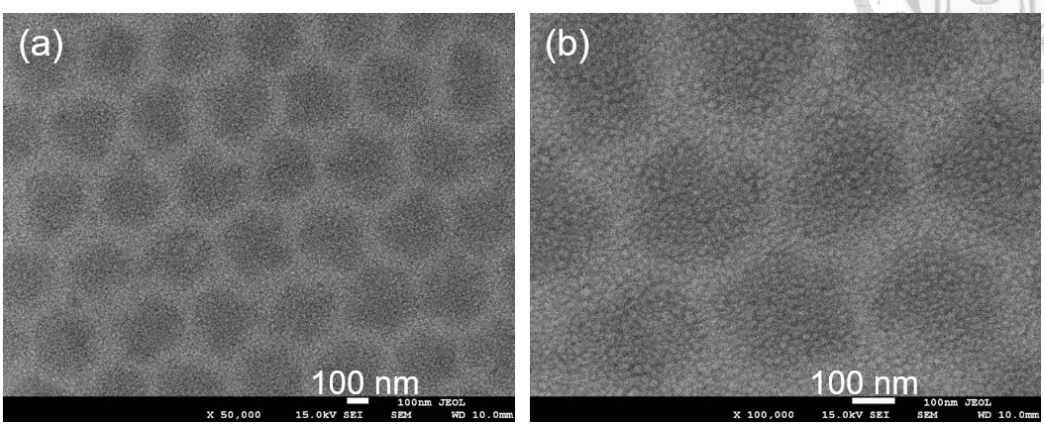

Fig. 5.4 (a) and (b): Plane-view SEM images with different magnifications of a test sample with Ag NP deposited onto the QD/PR filled surface shallow nano-holes.

doi:10.6342/NTU202203112

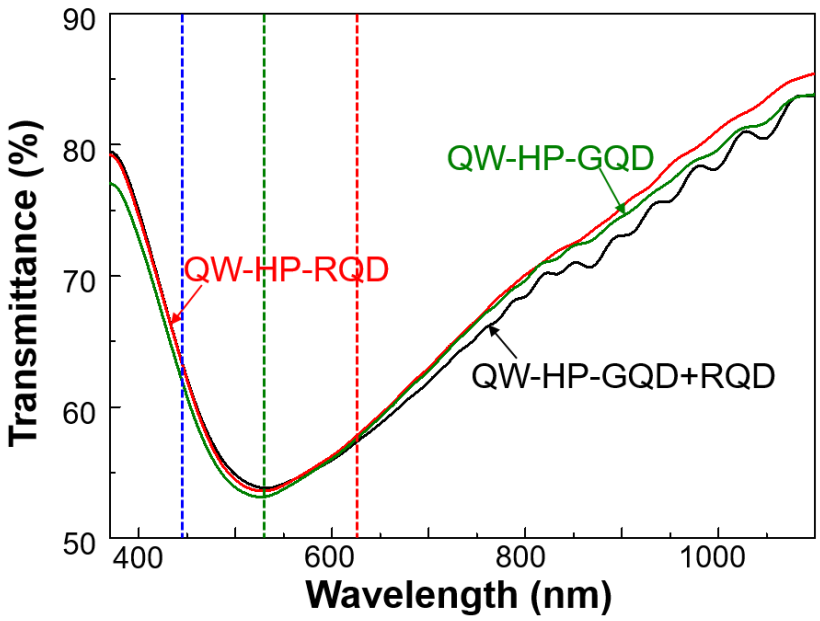

Fig. 5.5 Transmission spectra of the three samples after surface Ag NP deposition. The results are normalized with respect to those before Ag NP deposition. The three vertical dashed lines indicate the emission wavelengths of the QWs, GQD, and RQD.

doi:10.6342/NTU202203112

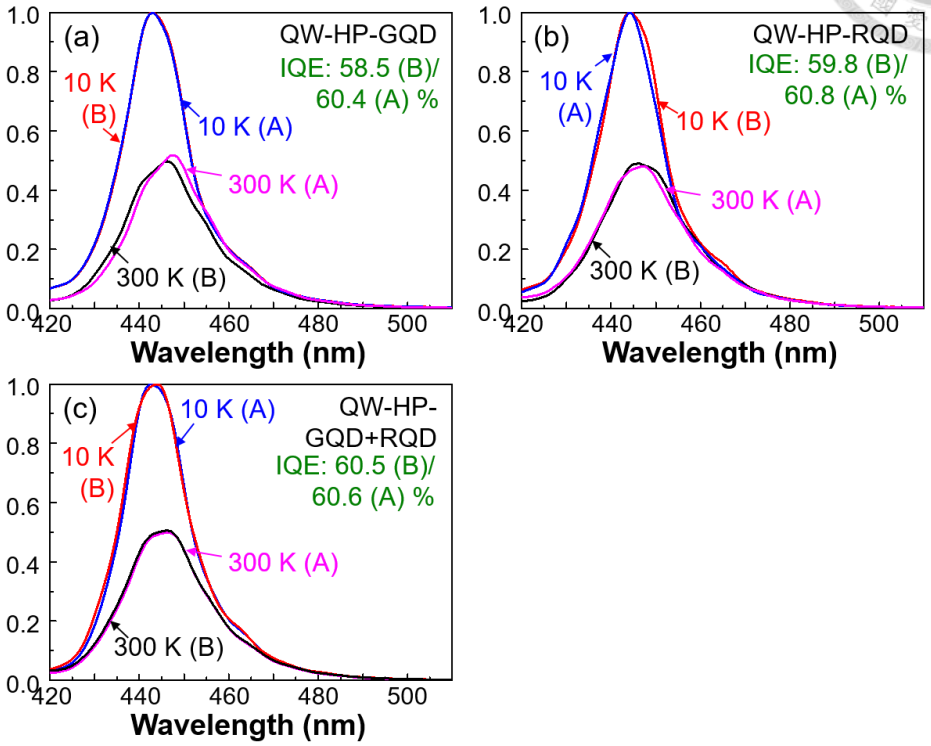

Fig. 5.6 (a)-(c): Normalized QW PL spectra of samples QW-HP-GQD, QW-HP-RQD, and QW-HP-GQD+RQD, respectively, before (B) and after (A) shallow nano-hole fabrication. The evaluated IQEs before (B) and after (A) shallow nano-hole fabrication are also shown in the figures.

doi:10.6342/NTU202203112

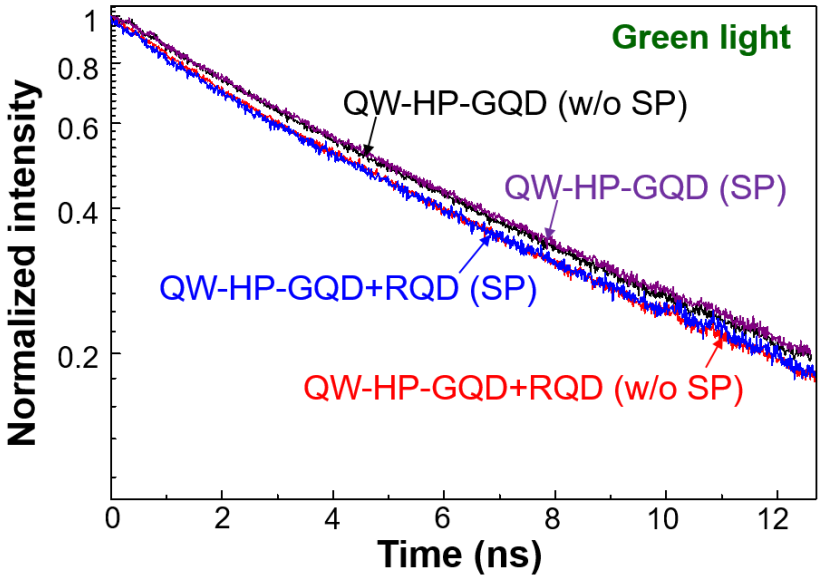

Fig. 5.7 Green-light PL decay profiles of samples QW-HP-GQD and QW-HP-GQD+RQD with and without SP coupling.

doi:10.6342/NTU202203112

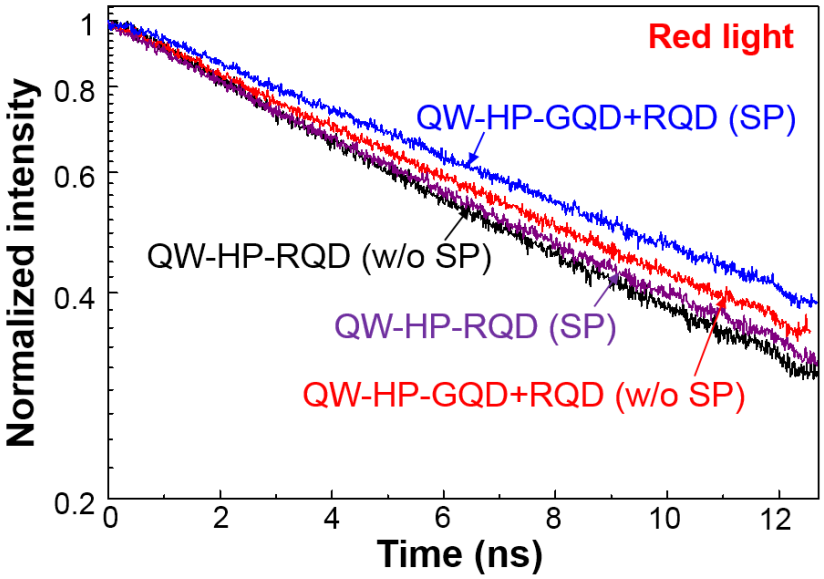

Fig. 5.8 Red-light PL decay profiles of samples QW-HP-RQD and QW-HP-GQD+RQD with and without SP coupling.

doi:10.6342/NTU202203112

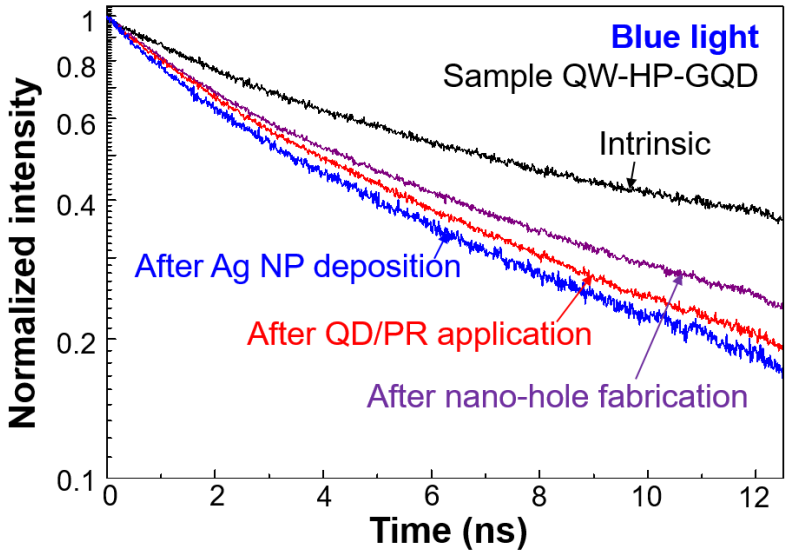

Fig. 5.9 Blue-light PL decay profiles of sample QW-HP-GQD in the intrinsic case and the cases after nano-hole fabrication, after QD/PR application, and after surface Ag NP deposition.

doi:10.6342/NTU202203112

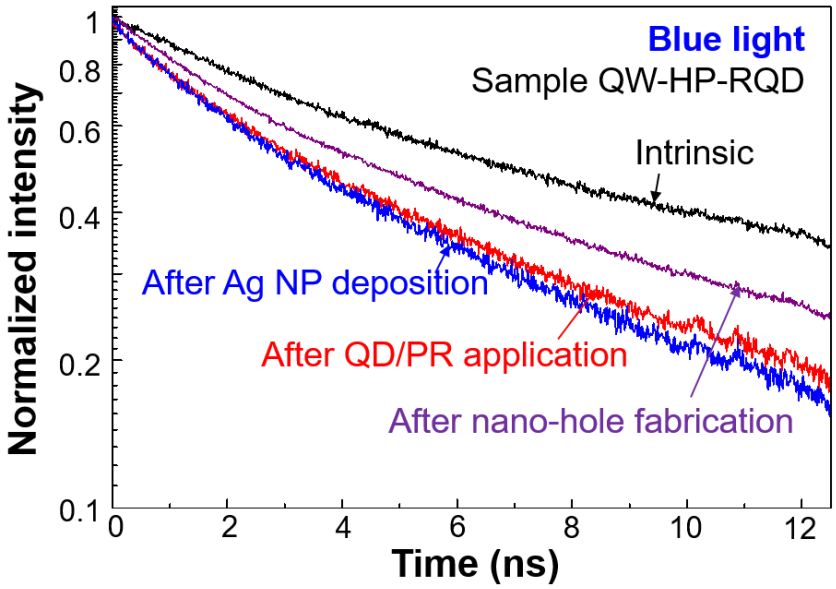

Fig. 5.10 Blue-light PL decay profiles of sample QW-HP-RQD in the intrinsic case and the cases after nano-hole fabrication, after QD/PR application, and after surface Ag NP deposition.

doi:10.6342/NTU202203112

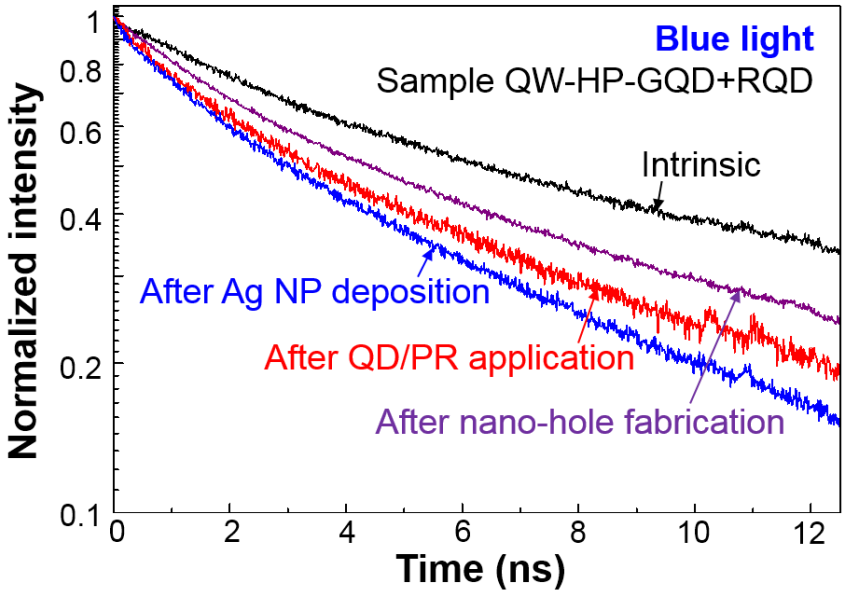

Fig. 5.11 Blue-light PL decay profiles of sample QW-HP-GQD+RQD in the intrinsic case and the cases after nano-hole fabrication, after QD/PR application, and after surface Ag NP deposition.

doi:10.6342/NTU202203112

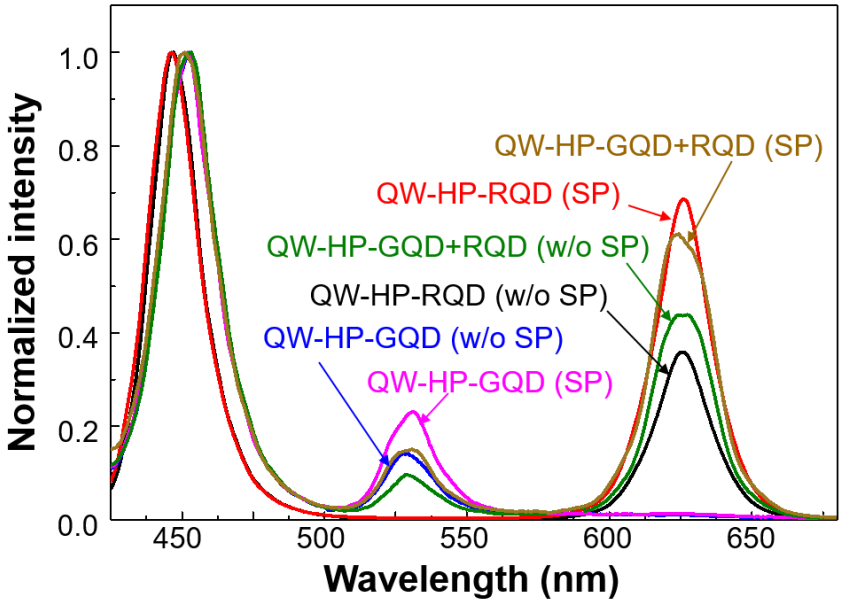

Fig. 5.12 Normalized PL spectra of samples QW-HP-GQD, QW-HP-RQD, and QW-HP-GQD+RQD with and without SP coupling. All the spectra are normalized with respect to the individual blue light intensities.

doi:10.6342/NTU202203112

Chapter 6 Discussions

It has been claimed that by inserting QDs into surface nano-holes such that they become closer to the embedded QWs, the FRET from the QWs into QDs can be enhanced for improving the color conversion efficiency, when compared the case that the QDs are placed on the sample top surface. Based on the study results above, this claim is true on a few conditions. First, the depth of the QW structure is larger than several tens nm; otherwise, the strength of the FRET from the QWs into the QDs on the top surface can be comparable to that from the QWs into the QDs inserted into the fabricated nano-holes. It is noted that the FRET form the QWs into the surface QDs occurs on the whole sample surface. However, the FRET from the QWs into the inserted QDs can occur only around the nano-hole sidewalls. Unless the surface nano-hole density is very high, the volume coverage of the former FRET can be larger than the latter, leading to a stronger FRET effect. Nevertheless, the fabrication of nano-holes leads to the generation of surface defect states, which enhance non-radiated recombination in the QWs. Therefore, the second condition is that the fabrication of the nano-holes does not significantly degrade the emission of the QWs, particularly the reduced emission volume does not create a crucial issue. The third condition to be considered is the size of the nano-hole. If the diameter or depth of the nano-hole is too large, most of the inserted QDs will not interact with the QWs for energy transfer. However, if the diameter of the nano-hole is too small, the quantity of inserted QDs becomes small such that the overall FRET effect is weak. Also, it may become difficult to insert QDs into the nano-hole.

It is noted that when we observe enhanced QD emission or FRET with QDs in the nano-holes, the enhancements are mainly caused by the nanoscale-cavity effect besides the shorter distance between the QWs and QDs. In a simulation study of this group, we have demonstrated the nanoscale-cavity effects on the QD emission and the FRET from the nearby QW portion into a QD. Such effects

doi:10.6342/NTU202203112

are highly polarization dependent. For maximizing such effects to optimize the color conversion process, the nano-hole geometry needs to be carefully designed. In particular, when synthesized Ag NPs are added to the system for inducing SP coupling, the nano-hole geometry is crucially important for optimizing the SP coupling effect.

doi:10.6342/NTU202203112

Chapter 7 Conclusions

In summary, we have experimentally demonstrated the enhancements of QD emission, FRET from GQD into RQD, FRET from embedded QW into QD, and SP coupling effect when QDs and synthesized Ag NPs were inserted into a surface nano-hole, which penetrated through the whole QW structure. We first fabricated nano-hole arrays on a GaN template to understand the effects without QW. Then, nano-hole arrays were fabricated on an InGaN/GaN QW template for studying the FRET processes from the QW into QD. The samples with planar top surfaces for overlaying QDs were also prepared to compare the results with the nano-hole samples. Meanwhile, we compared the results of a set of sample with deeper nano-holes with those with shallower nano-holes. The overall FRET from the QW structure into the inserted QDs in a shallower nano-hole sample was relatively stronger. Finally, we investigated the SP coupling effect of surface Ag NPs on the FRET from the QW structure into the QDs inserted into a shallow nano-hole. The FRET process was indeed enhanced through the SP coupling effect.

doi:10.6342/NTU202203112

References:

1. E. Jang, S. Jun, H. Jang, J. Lim, B. Kim, and Y. Kim, "White-light-emitting diodes with quantum dot color converters for display backlights," Adv. Mater. **22**(28), 3076-3080 (2010).
2. H. C. Yoon, H. Kang, S. Lee, J. H. Oh, H. Yang, and Y. R. Do, "Study of perovskite QD down-converted LEDs and six-color white LEDs for future displays with excellent color performance," ACS Appl. Mater. Interfaces **8**(28), 18189-18200 (2016).
3. C. Du, Z. Ma, J. Zhou, T. Lu, Y. Jiang, P. Zuo, H. Jia, and H. Chen, "Enhancing the quantum efficiency of InGaN yellow-green light-emitting diodes by growth interruption," Appl. Phys. Lett. **105**(7), 071108 (2014).
4. X. Zhao, B. Tang, L. Gong, J. Bai, J. Ping, and S. Zhou, "Rational construction of staggered InGaN quantum wells for efficient yellow light-emitting diodes," Appl. Phys. Lett. **118**(18), 182102 (2021).
5. J. H. Oh, K. H. Lee, H. C. Yoon, H. Yang, and Y. R. Do, "Color-by-blue display using blue quantum dot light-emitting diodes and green/red color converting phosphors," Opt. Express **22**(S2), A511-A520 (2014).
6. H. V. Han, H. Y. Lin, C. C. Lin, W. C. Chong, J. R. Li, K. J. Chen, P. Yu, T. M. Chen, H. M. Chen, K. M. Lau, and H. C. Kuo, "Resonant-enhanced full-color emission of quantum-dot-based micro LED display technology," Opt. Express **23**(25), 32504-32515 (2015).
7. T. Förster, "Energy transport and fluorescence," Naturwissenschaften **33**, 166-175 (1946).
8. M. Achermann, M. A. Petruska, S. Kos, D. L. Smith, D. D. Koleske, and V. I. Klimov, "Energy-transfer pumping of semiconductor nanocrystals using an epitaxial quantum well," Nature **429**(6992), 642-646 (2004).

doi:10.6342/NTU202203112

9. J. Yu, L. Wang, D. Yang, Z. Hao, Y. Luo, C. Sun, Y. Han, B. Xiong, J. Wang, and H. Li, "Improving the internal quantum efficiency of green InGaN quantum dots through coupled InGaN/GaN quantum well and quantum dot structure," Appl. Phys. Express **8**(9), 094001 (2015).
10. Y. P. Chen, C. C. Ni, R. N. Wu, S. Y. Kuo, Y. C. Su, Y. Y. Huang, J. W. Chen, Y. C. Hsu, S. H. Wu, C. Y. Chen, P. H. Wu, Y. W. Kiang, and C. C. Yang, "Combined effects of surface plasmon coupling and Förster resonance energy transfer on the light color conversion behaviors of colloidal quantum dots on an InGaN/GaN quantum-well nanodisk structure," Nanotechnology **32**(13), 135206 (2021).
11. C. C. Ni, S. Y. Kuo, Z. H. Li, S. H. Wu, R. N. Wu, C. Y. Chen, and C. C. Yang, "Förster resonance energy transfer in surface plasmon coupled color conversion processes of colloidal quantum dots," Opt. Express **29**(3), 4067-4081 (2021).
12. S. Chanyawadee, P. G. Lagoudakis, R. T. Harley, M. D. B. Charlton, D. V. Talapin, H. W. Huang, and C. H. Lin, "Increased color-conversion efficiency in hybrid light-emitting diodes utilizing non-radiative energy transfer," Adv. Mater. **22**(5), 602-606 (2010).
13. C. Krishman, M. Brossard, K.-Y. Lee, J.-K. Huang, C.-H. Lin, H.-C. Kuo, M. D. B. Charlton, and P. G. Lagoudakis, "Hybrid photonic crystal light-emitting diode renders 123% color conversion effective quantum yield," Optica **3**(5), 503-509 (2016).
14. Z. Zhuang, X. Guo, B. Liu, F. Hu, Y. Li, T. Tao, J. Dai, T. Zhi, Z. Xie, P. Chen, D. Chen, H. Ge, X. Wang, M. Xiao, Y. Shi, Y. Zheng, and R. Zhang, "High color rendering index hybrid III-nitride/nanocrystals white light-emitting diodes," Adv. Funct. Mater. **26**(1), 36-43 (2016).
15. M. Athanasiou, P. Papagiorgis, A. Manoli, C. Bernasconi, N. Poyiatzis, P.-M. Coulon, P. Shields, M. I. Bodnarchuk, M. V. Kovalenko, T. Wang, and G. Itskos, "InGaN nanohole arrays coated by

doi:10.6342/NTU202203112

lead halide perovskite nanocrystals for solid-state lighting," ACS Appl. Nano Mater. **3**(3), 2167-2175 (2020).

16. R. Wan, G. Li, X. Gao, Z. Liu, J. Li, X. Yi, N. Chi, and L. Wang, "Nanohole array structured GaN-based white LEDs with improved modulation bandwidth via plasmon resonance and non-radiative energy transfer," Photon. Res. **9**(7), 1213-1217 (2021).
17. Z. Du , D. Li, W. Guo, F. Xiong, P. Tang, X. Zhou, Y. Zhang, T. Guo, Q. Yan, and J. Sun, "Quantum dot color conversion efficiency enhancement in micro-light-emitting diodes by non-radiative energy transfer," IEEE Electron Dev. Lett. **42**(8), 1184-1187 (2021).
18. A. Neogi, C. W. Lee, H. O. Everitt, T. Kuroda, A. Tackeuchi, and E. Yablonvitch, "Enhancement of spontaneous recombination rate in a quantum well by resonant surface plasmon coupling," Phys. Rev. B. **66**, 153305 (2002).
19. K. Okamoto, I. Niki, A. Shvartser, Y. Narukawa, T. Mukai, and A. Scherer, "Surface-plasmon-enhanced light emitters based on InGaN quantum wells," Nature Mater. **3**, 601 (2004).
20. M. K. Kwon, J. Y. Kim, B. H. Kim, I. K. Park, C. Y. Cho, C. C. Byeon, and S. J. Park, "Surface-plasmon-enhanced light-emitting diodes," Adv. Mater. **20**, 1253 (2008).
21. H. A. Atwater and A. Polman, "Plasmonics for improved photovoltaic devices," Nature Mater. **9**, 205 (2010).
22. J. Zhu, C. M. Hsu, Z. Yu, S. Fan, and Y. Cu, "Nanodome solar cells with efficient light management and self-cleaning," Nano Lett. **10**, 1979 (2010).
23. E. M. Purcell, "Spontaneous emission probabilities at radio frequencies," Phys. Rev. **69**, 681-681 (1946).
24. Y. Kuo, S. Y. Ting, C. H. Liao, J. J. Huang, C. Y. Chen, C. Hsieh, Y. C. Lu, C. Y. Chen, K. C. Shen, C. F. Lu, D. M. Yeh, J. Y. Wang, W. H. Chuang, Y. W. Kiang, and C. C. Yang, "Surface

doi:10.6342/NTU202203112

plasmon coupling with radiating dipole for enhancing the emission efficiency of a light-emitting diode," Opt. Express **19**, A914 (2011).

25. C. Y. Su, C. H. Lin, Y. F. Yao, W. H. Liu, M. Y. Su, H. C. Chiang, M. C. Tsai, C. G. Tu, H. T. Chen, Y. W. Kiang, and C. C. Yang, "Dependencies of surface plasmon coupling effects on the p-GaN thickness of a thin-p-type light-emitting diode," Opt. Express **25**, 21526-21536 (2017).
26. C. F. Lu, C. H. Liao, C. Y. Chen, C. Hsieh, Y. W. Kiang, and C. C. Yang, "Reduction of the efficiency droop effect of a light-emitting diode through surface plasmon coupling," Appl. Phys. Lett. **96**, 261104 (2010).
27. C. H. Lin, C. Y. Su, E. Zhu, Y. F. Yao, C. Hsieh, C. G. Tu, H. T. Chen, Y. W. Kiang, and C. C. Yang, "Modulation behaviors of surface plasmon coupled light-emitting diode," Opt. Express **23**, 8150 (2015).
28. C. J. Cai, Y. T. Wang, C. C. Ni, R. N. Wu, C. Y. Chen, Y. W. Kiang, and C. C. Yang, "Emission behaviors of colloidal quantum dots linked onto synthesized metal nanoparticles," Nanotechnology **31**, 095201 (2020).
29. Y. T. Wang, C. W. Liu, P. Y. Chen, R. N. Wu, C. C. Ni, C. J. Cai, Y. W. Kiang, and C. C. Yang, "Color conversion efficiency enhancement of colloidal quantum dot through its linkage with synthesized metal nanoparticle on a blue light-emitting diode," Opt. Lett. **44**, 5691-5694 (2019).
30. W. Y. Chang, Y. Kuo, Y. W. Kiang, and C. C. Yang, "Simulation study on light color conversion enhancement through surface plasmon coupling," Opt. Express **27**, A629-A642 (2019).
31. C. H. Lin, H. C. Chiang, Y. T. Wang, Y. F. Yao, C. C. Chen, W. F. Tse, R. N. Wu, W. Y. Chang, Y. Kuo, Y. W. Kiang, and C. C. Yang, "Efficiency enhancement of light color conversion through surface plasmon coupling," Opt. Express **26**, 23629 (2018).

doi:10.6342/NTU202203112

32. Y. Y. Huang, Z. H. Li, Y. C. Lai, J. C. Chen, S. H. Wu, S. Yang, Y. Kuo, C. C. Yang, T. C. Hsu, and C. L. Lee, "Nanoscale-cavity enhancement of color conversion with colloidal quantum dots embedded in surface nano-holes of a blue-emitting light-emitting diode," submitted to Nanotechnology.
33. C. A. J. Lin, R. A. Sperling, J. K. Li, T. A. Yang, P. Y. Li, M. Zanella, W. H. Chang, and W. J. Parak, "Design of an amphiphilic polymer for nanoparticle coating and functionalization," Small **4**(3), 334-341 (2008).
34. S. Lin, G. Tan, J. Yu, E. Chen, Y. Weng, X. Zhou S. Xu, Y. Ye, Q. F. Yan, and T. Guo, "Multi-primary-color quantum-dot down-converting films for display applications," Opt. Express **27**(20), 28480-28493 (2019).
35. S. Lee and C. Lee, "High-density quantum dots composites and its photolithographic patterning applications," Polym. Adv. Technol. **30**(3), 749-754 (2019).
36. Y. Liu, Z. Wang, Y. Liu, G. Zhu, O. Jacobson, X. Fu, R. Bai, X. Lin, N. Lu, X. Yang, W. Fan, J. Song, Z. Wang, G. Yu, F. Zhang, H. Kalish, G. Niu, Z. Nie, and X. Chen, "Suppressing nanoparticle-mononuclear phagocyte system interactions of two-dimensional gold nanorings for improved tumor accumulation and photothermal ablation of tumors," ACS Nano **11**(10), 10539-10548 (2017).
37. M. Uz, V. Bulmus, and S. A. Altinkaya, "Effect of PEG grafting density and hydrodynamic volume on gold nanoparticle - cell interactions: An investigation on cell cycle, apoptosis, and DNA damage," Langmuir **32**(23), 5997-6009 (2016).

doi:10.6342/NTU202203112